Energy Reports 13 (2025) 1384–1399

Contents lists available at ScienceDirect

Energy Reports

journal homepage: www.elsevier.com/locate/egyr

Research paper

Incremental neuroconductance to analyze performance losses due to soiling in photovoltaic generators

Ernesto Palo-Tejada [a], Victoria Campos-Falcon [a], Jan Amaru Töfflinger [b,*]

[a] Departamento Académico de Física, Universidad Nacional de San Agustín de Arequipa, Peru
[b] Departamento de Ciencias, Sección Física, Pontificia Universidad Católica del Perú, Peru

ARTICLE INFO

Keywords:
PV modules
Soiling
Artificial neural networks
Energy loss estimation

ABSTRACT

Many large photovoltaic plants are being installed in desert regions with very high solar irradiation but are subject to significant losses due to soiling. Quantifying soiling losses in energy production is crucial for optimizing cleaning schedules and the plants' bankability but can be challenging, particularly when knowledge about soiling losses is desired before plant implementation. This work introduces an innovative, self-contained, and easily deployable system that quantifies energy losses from dust accumulation on photovoltaic arrays. Our approach, termed 'Incremental Neuroconductance,' combines a photovoltaic module, irradiance, and module temperature sensors with a calibrated electrical model and a trained artificial neural network. The models estimate the clean module's maximum power output based on the measured irradiance and module temperature. The system simultaneously measures the module's maximum power by using maximum power point tracking based on the incremental conductance method. Under clean module conditions, the models and measurements yield identical power values. However, once the module starts accumulating dust, the measurements yield lower power values than predicted by the electrical model and the neural network, quantifying the power loss due to soiling. We assess and contrast the precision of the electrical and the artificial neural network models in estimating the clean module's power, emphasizing the importance of their calibration and training using experimental data. Our findings reveal comparable performances between the two models, with the trained neural network offering lower computational costs. Model recalibration and retraining can compensate for long-term module degradation. We report on the results from one year of system operation, demonstrating its capability to predict performance losses due to the soiling of the photovoltaic module without requiring the implementation of a complete photovoltaic system or plant. Over the year, maintaining a monthly cleaning schedule, the system estimates a 7 % energy loss due to soiling for a photovoltaic array located in the desertic region of Arequipa, Peru.

1. Introduction

Most of the large photovoltaic (PV) plants in the coming years will be installed in desertic areas with maximum irradiation worldwide, but which are subject to high losses due to soiling, such as in China, India, Peru, Chile (Vásquez et al., 2019). In desert areas such as the southern coast of Peru and northern Chile, the modules suffer from the harshness of environmental factors leading to exceptionally high soiling rates (Ilse et al., 2018a; Maghami, et al., 2016; Cordero, et al., 2018). They are among the most desertic areas in the world, with cloud cover rates of less than 3 % (Olivares, et al., 2020). These desert areas receive the highest levels of solar radiation worldwide, and it has been documented that global horizontal irradiation exceeds $2500 kWh/m^2$ per year (Escobar Moragas et al., 2015). Radiative factors condition the climate in these desert areas. The intense solar radiation makes them ideal for PV energy generation. However, the almost total absence of precipitation and the arid environmental conditions generate dust or dirt on the PV modules, which can have a drastic short-term influence on the energy performance of PV modules, reaching more than 1 % power loss per day (Ilse et al., 2018b; Ilse, et al., 2019). Soiling is a complex phenomenon that differs markedly depending on location and is influenced by many factors, such as the concentration of dust in the air, the frequency of precipitation, the tilt angle of the PV module, the site specifications, the speed of the wind or relative humidity, and dew formation (Ilse et al.,

* Corresponding author.
E-mail address: japalominot@pucp.edu.pe (J.A. Töfflinger).

https://doi.org/10.1016/j.egyr.2025.01.009
Received 14 July 2023; Received in revised form 31 December 2024; Accepted 4 January 2025
Available online 15 January 2025

2018b; Ilse, et al., 2019).

Soiling can affect the PV system's performance through two main mechanisms: First, the dust attenuates the amount of solar irradiance that reaches the solar cells for PV conversion (Javed et al., 2020; Zhang, et al., 2020; Luque et al., 2018; Chanchangi et al., 2021). For instance, the module's optical response depends on the dust particles' size and morphology (Jathar, et al., 2023). Second, the dust deposition on the top surface of the PV modules can cause material degradation. Depending on the local environmental conditions and the module tilt angle, both mechanisms can co-occur depending on the interaction between dust particles and module surfaces.

Dirt on PV modules is typically inhomogeneous due to dust accumulation on the edges or corners of the PV modules, depending on the installation and wind profiles, as demonstrated by (Gostein et al., 2015). Due to the series interconnection of the solar cells in standard PV modules, non-homogeneous soiling causes a high current imbalance. Consequently, it causes significant power loss and local heating of the PV modules due to partial shading (Koirala et al., 2009; Deng, et al., 2017; Daliento et al., 2016; Hanifi et al., 2015; Spanoche et al., 2012). Therefore, the losses in the output power of a non-homogeneously dirty PV module can be larger than expected for the same amount of dust spread homogeneously on the surface (Maghami, et al., 2016).

A study carried out in the northern Atacama desert of Chile (Olivares, et al., 2017) reported that the particles deposited on the PV modules are less than 63 μm in size, and after four months of dust accumulation, the transmittance of the photovoltaic glass was reduced by 55 %. In (Olivares, et al., 2020), an asymptotic behavior was observed in the accumulated density of surface dust for six months. They explained that as the glass got dirty, the probability of glass-particle interaction decreased in favor of particle-to-particle interaction. The monthly dust accumulation on the surface was up to $0.17 mg/cm^2$, causing current losses of 19 % after four months. This, in turn, led to a 13.5 % reduction in overall efficiency. Other desertic regions in the world experience similar problems. For example, (Almasoud and Gandayh, 2015) determined the dirt losses of PV modules installed in Shiraz, Iran. For measurement, PV modules were installed with a tilt angle of 30°. The short-circuit current of each module, wind speed, ambient humidity, ambient temperature, module temperature, and solar radiation were continuously measured during the experiment period. The results indicated that the average daily loss over eight weeks of exposure was 4.45 % due to soiling. A recent and more extensive study in Iran (Dehshiri and Firoozabadi, 2023) shows that dust accumulation can considerably reduce the levelized cost of energy (LCOE). However, an optimized cleaning program can reduce LCOE losses. The authors state that a cleaning schedule that takes into account losses due to dust accumulation is a vital solution to developing solar energy in dusty areas. In a study conducted in the city of Medina, Saudi Arabia, (Benghanem et al., 2018) recorded 28 % losses due to the effects of dust accumulation for 60 days on the surface of PV modules. In their work, an intelligent cleaning system was proposed, using the notion of dust density, to start cleaning when an inadmissible value of power loss is reached.

However, detecting dust accumulation is challenging due to the unique conditions at any dusty geographic location, such as industrial emissions and environmental pollution (Rahman et al., 2018; Zhang, et al., 2021). The standard technique to quantify soiling losses is measuring the temperature-compensated short-circuit current of two identical modules. One reference module is manually or automatically cleaned; the other, the test module, is allowed to accumulate dust, presumably at the same rate as the photovoltaic generator. This method uses the fact that the short-circuit current is proportional to the irradiance reaching the module and that the power produced is a known function of the irradiance. This method is described in (Caron and Littmann, 2012). However, in the devices that compare the short-circuit current of two photovoltaic modules, it is assumed that these must be identical and be in the same conditions of irradiance and temperature when the short-circuit current is measured. This method does not consider the clouds' influence, the sun's zenith angle, the level of irradiance in both modules, and the variation of the spectral distribution. Furthermore, it is not only the amount of dust or dirt on the module that affects the short-circuit current. The distribution of dust on the module can produce different results of short-circuit current. Since non-uniform distributions of dust on the module are frequent and occur due to the influence of module orientation, wind, rain, and gravity, which results in dust accumulation on the module's edges. Another disadvantage of the method described above is that it requires one of the modules to be cleaned daily with the consequent cost. Alternatively, an automatic water cleaning system can be used, but water lines are usually unavailable at the installation sites of large photovoltaic plants, which would imply transporting and maintaining water tanks in remote places, creating additional maintenance costs.

There are other devices to measure the dirt index in photovoltaic modules, such as the CR-PVS1 marketed by Campbell Scientific, the DustIQ by Kipp&Zonen, or the devices described in (Muller, et al., 2021) and (Fan et al., 2021). A dust sensor, such as the DustIQ system by Kipp&Zonen, can estimate dust concentration using reflectance measurements (Korevaar et al., 2017). However, these devices do not quantify the PV energy lost due to soiling.

Alternatively, in (Smestad, et al., 2020), the authors propose a model to estimate PV dust losses through optical characterization and suggest a linear relationship between dust coverage rate and transmittance. Quantitative detection of dust concentration on photovoltaic modules is a complex problem. Two methods are commonly used in the laboratory to measure dust concentration, including direct and indirect measurements (Zaihidee et al., 2016). In the direct measurement method, the dust of PV modules is collected in distilled water, and the weight of the dust is obtained by filtering, drying, and weighing. The indirect measurement method compares the difference in weight between clean and dirty PV modules, obtaining the dust concentration indirectly (Hegazy, 2001; Beattie, et al., 2012; Jiang et al., 2011). However, this indirect method requires access to specialized laboratories and cannot be performed in real-time.

Machine learning (ML) methods have been used to measure and detect dust. (Igathinathane, et al., 2009) use computer vision to measure the length and width of dust particles in the air and determine the size distribution of the particles in high-resolution images of PV module surfaces. (Proietti et al., 2015) described a method for dust detection and analysis based on the k-nearest neighbors (K-NN) method to identify the shape of dust particles and the accumulation rate. In general, ML methods were mainly used for particle shape analysis and classification. In (Fan et al., 2021), the authors use an image analysis method to determine the state of dust in PV modules by proposing a new deep residual neural network (DRNN) model to determine the concentration of dust on the module. However, these indirect methods require complex calibrations with high computational cost for image processing and do not quantify the module power loss.

Soiling losses can also be quantified by measuring the overall efficiency of the PV plant and comparing this to the expected performance under given meteorological conditions. This method is used, for example, in (Kimber et al., 2006). A comparison of output power is typically used to evaluate the effect of dust accumulation on PV output. The level of dust accumulation can be estimated by calculating the ratio between actual and rated output power. (Kaldellis and Kapsali, 2011) established a general exponential model to analyze the relationship between dust accumulation on PV modules and the photoelectric conversion efficiency. (Alnaser, et al., 2015) proposed a model that relates the output power and the dust concentration in outdoor conditions based on experimental verification. (Fan et al., 2021) propose a coupling model of dust concentration and photoelectric conversion efficiency (DC-PCE), considering the irradiance level and dust types. However, these methods require access to the power data of a PV system, which may not be feasible for many power plants. Furthermore, for this

analysis, the PV plant has to be already operational; thus, this method does not allow for a soiling analysis prior to the plant installation or operation.

Other factors, such as the aging and degradation of the modules, also result in performance losses in photovoltaic arrays. Most of the above-mentioned methods cannot be applied in this case because they assume that all losses are due to meteorological conditions. Nor can all these methods be used to assess yield losses before plant construction. For example, in (Abraim, et al., 2023), the authors affirm that a priori knowledge about the phenomenon of dirt in a specific site allows for predicting the performance and profitability of the solar project. The study concurs that the recovery of losses due to dirt begins with installing a reliable soil monitoring system, followed by implementing optimized cleaning or soil mitigation procedures.

To obtain the maximum electrical power of a PV generator, a wide variety of maximum power point tracking (MPPT) algorithms have been proposed; most publications agree that they can be classified into four groups: traditional algorithms, optimization algorithms, artificial intelligence algorithms, and hybrid algorithms (Senthilkumar, et al., 2023). Among the traditional algorithms, the perturb and observe (P&O) and the incremental conductance algorithms stand out due to their simplicity and, thus, extensive application (Thakurta, 2020; Zhao et al., 2021; Senniappan and Umapathy, 2021; Shang et al., 2020; Kim et al., 2020). Optimization-based algorithms perform better with respect to tracking speed, accuracy, and searchability. Examples of these algorithms are particle swarm optimization (PSO), grey wolf optimization (GWO), and cuckoo search (CS) (Obukhov et al., 2020; Gude et al., 2022). Artificial intelligence algorithms, such as those based on neural networks, react to small changes in irradiance and temperature (Krithiga et al., 2023; Sivamani and Mohan, 2022). Hybrid algorithms combine the best features of the previous ones, resulting in improved efficiency, tracking speed, reduction of oscillations, power loss, and shorter convergence time (Krithiga et al., 2023).

In summary, the above-mentioned methods for estimating soiling losses in PV systems face significant limitations. Short-circuit current measurements assume identical conditions and overlook environmental variations and non-uniform dust distribution, while commercial devices estimate dust concentration but fail to quantify energy losses. Optical characterization and laboratory-based methods are impractical for real-time or field applications. Machine learning approaches require high computational costs and complex calibrations. Performance comparison methods depend on operational data and cannot assess pre-construction losses. Additionally, water scarcity, inhomogeneous dust accumulation, and site-specific environmental factors further challenge the accuracy and applicability of these methods, emphasizing the need for more versatile solutions.

This paper introduces a self-contained, portable system designed to address the limitations of the previously mentioned methods for estimating soiling losses in PV systems. This system facilitates soiling analysis both before implementation and during the operation of PV systems. It can account for spatial inhomogeneities of dust accumulation and the long-term degradation of PV modules through recalibration and retraining. The proposed system and method, named Incremental Neuroconductance, integrates an artificial neural network (ANN), an electrical model, and MPPT based on incremental conductance. This combination allows for estimating daily energy losses due to soiling in a PV array with minimal maintenance requirements.

We tested the device over a one-year period in Arequipa, Peru, a region that has a desert climate characterized by very high irradiation, very low relative humidity, high temperatures, and atmospheric dust content. These conditions are typical of the Arid Diagonal, a contiguous zone of arid and semi-arid climate that runs through South America from the coast of Peru in the northwest to Argentine Patagonia in the southeast, including large swathes of Bolivia and Chile. These desert regions have emerged as ideal locations for GW-scale photovoltaic installations due to the large tracts of unused land, abundant hours of high-irradiation sunshine, and clear skies (Adothu et al., 2024). For instance, Arequipa and its neighboring regions, such as Ica, Moquegua, and Tacna, currently operate Peru's largest PV plants. According to Peru's Regulatory Agency for Investment in Energy and Mining (Osinergmin, 2024), by 2028, these four desert regions in southern Peru will exceed 9 GW of installed PV utility-scale capacity, making up about 90 % of the country's total PV capacity. However, the harsh desert climate presents challenges to the reliability and financial viability of these projects, mainly due to the high concentration of atmospheric dust and the high temperatures that modules can reach. In this work, we are interested precisely in climatic zones such as those existing in this part of the world, so it is of interest to have devices such as the one we propose to evaluate the technical and economic viability of photovoltaic exploitation in these extreme climates. These PV plants would greatly benefit from experimental information on the energy losses caused by soiling.

2. Methodology

In this chapter, we begin by providing an overview of the system's components and the procedures for calibrating and training the models. Subsequently, in the ensuing subchapters, we delve into a more detailed description of the functionality of the primary components, measurements, and algorithms.

Fig. 1(a) shows a photo of the developed Incremental Neuroconductance PV (INC-PV) system and Fig. 1(b) its corresponding block diagram, which consists of the following elements: (1) A 5W monocrystalline silicon PV test module, based in back surface field (BSF) solar cells, (2) DC-DC single-ended primary inductance converter (SEPIC), (3) Pyranometer, (4) Module temperature sensors, (5) Instrumentation, (6) Neural Network.

First, the system undergoes training and calibration under clean module conditions:

1. For the construction of the ANN training set, the clean PV module operates at its maximum power point (MPP), which the SEPIC and the incremental conductance algorithm determine. The PWM (pulse width modulation) is generated by the BCM2711 chip included in raspberry-pi4, the operating frequency is 20Khz and the duty cycle between 20 % and 80 % is controlled by the incremental conductance algorithm, the PWM signal opens and closes the N-channel mosfet of the ZPIC, as shown in Fig. 1. We employ artificial intelligence techniques, utilizing an ANN with inputs including the time of day, measured module temperature (T), and irradiance (G) on the test module. The ANN comprises two hidden layers, each with 14 neurons and one neuron in the output layer.
2. We measure the voltage (V) and current (I) at maximum power as output parameters. The ANN is trained by utilizing these data and the Root Mean Squared Propagation (RMSprop) algorithm, as described in (Tieleman et al., 2012). Subsequently, the system employs the trained neural network to estimate the maximum power delivered by the module under any given time (H), temperature, and irradiance condition.
3. Simultaneously, using the same training set as utilized in the ANN, we calibrate an electrical model of the PV test module under the specified operating conditions (Piliougine, et al., 2021). This calibrated model is then employed to estimate the module's maximum power under the given module temperature and irradiance conditions.

Next, utilizing the trained system, an experimental campaign is initiated to measure power losses resulting from the accumulation of dust or dirt on the PV generator, as outlined below:

1. The PV module is allowed to accumulate dust or dirt at the expected rate for a PV array. Concurrently, using the DC-DC SEPIC in

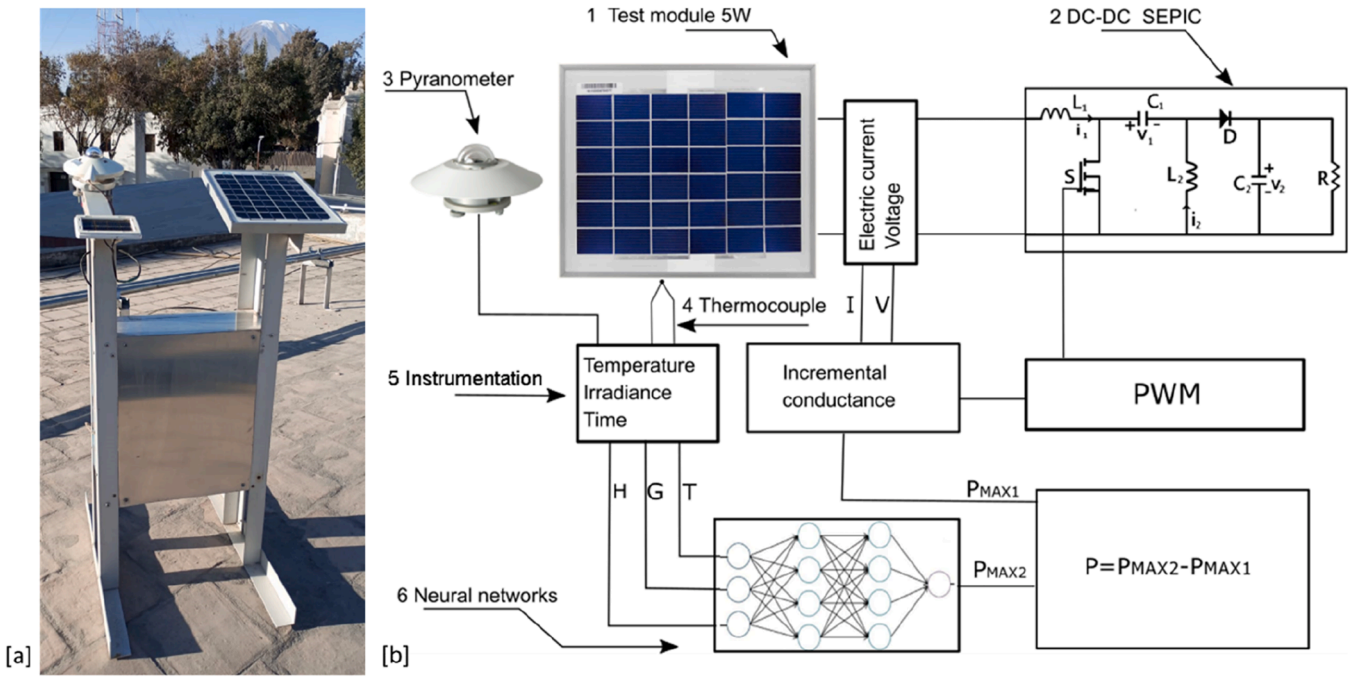

Fig. 1. (a) Photo of the INC-PV system. (b) INC-PV Instrument Block Diagram, where H is the time of day, G the irradiance, T the module temperature, V and I are the maximum power voltage and current, respectively.

conjunction with an incremental conductance MPPT algorithm (Rezvanyvardom and Mirzaei, 2020), the system measures the maximum power P_{MAX1} delivered by the test module under the given conditions of irradiance, temperature, and soiling.

2. The system obtains the irradiance and temperature measurements of the test module, serving as inputs to the previously trained neural network and the calibrated electrical model. The output yields the calculated maximum power P_{MAX2}.
3. As the ANN was trained and the electrical model calibrated with the completely clean test PV module, both models predict the maximum power delivered by the clean test module under the prevailing irradiance and temperature conditions.
4. The power loss due to dirt is estimated as follows: $P_{loss} = P_{MAX2}–P_{MAX1}$.
5. Finally, the effectiveness of the ANN and the electrical model is compared.

For data processing, the system uses a 28 nm ARM Cortex-172 processor with four cores at 1.5 GHz, a Deben-Linux operating system, and software to estimate the power of the electrical model, and the ANN is written in Python 3.7.6 64-bit. The electrical model is implemented on the well-known numpy-1.216 library, and the ANN is implemented on the tensorflow-2.5.0 library.

2.1. The photovoltaic module as a dust sensor

One of the primary sensors in our setup is the 5 W monocrystalline silicon module illustrated in Fig. 1(b) – denoted as element 1. The manufacturer's provided electrical specifications for this module are detailed in Table 1. Under ideal conditions of irradiance and temperature, when the module is devoid of dust or debris, we regulate the DC-DC load using pulse width modulation (PWM) to ensure the module operates at its maximum power output (Chatterjee and Das, 2023). However, if dust accumulates on the module's surface, the maximum power output diminishes compared to its clean state.

The maximum power output achievable by the clean module can be estimated in two manners: through a calibrated electrical model of the module and via a trained neural network. Conversely, the maximum experimental power output attained under dirty conditions can be directly measured. The disparity between these two values is leveraged to quantify the energy loss attributable to soiling.

Table 1
Monocrystalline silicon PV module electrical parameters at standard test conditions (STC).

Electrical parameter	Symbol	Value
Maximum power	P_{mp}	5 W
Voltage at maximum power	V_{mp}	17,5 V
Current at maximum power	I_{mp}	0,29 A
Open-circuit voltage	V_{oc}	21,5 V
Current at maximum power	I_{sc}	0,31 A
Current temperature coefficient	μ_{sc}	$0{,}124 \times 10^{-3}$ A/K
Number of cells	Ns	36

2.2. Incremental conductance method

For this work, the implemented incremental conductance method (IncCond) was chosen due to its simplicity and effectiveness. This method operates on the premise that the slope of the P-V curve of a photovoltaic system is zero at the maximum power point (MPP), positive to the left of the MPP, and negative to the right (Karami et al., 2017). Fig. 2 shows the respective flowchart.

The MPP is determined through a comparison between the instantaneous conductance (I/V) and the IncCond ($\Delta I/\Delta V$). Subsequently, the PWM is adjusted to attain the MPP, as illustrated in the flowchart depicted in Fig. 2. Once the MPP is attained, the system operates at this point until it detects a variation in ΔI, which can be induced by fluctuations in weather conditions. Upon such detection, the PWM pulse width D is modified iteratively to realign with the MPP using the formula $D(n+1) = D(n) + \Delta D$. A drawback of the IncCond method is that if the increment ΔD is small, the system's response to reach MPP is slow. However, employing variable increments ΔD allows for a rapid convergence to the MPP. Moreover, the IncCond method exhibits reduced oscillatory behavior around the MPP in comparison to the P&O method (Salas et al., 2006).

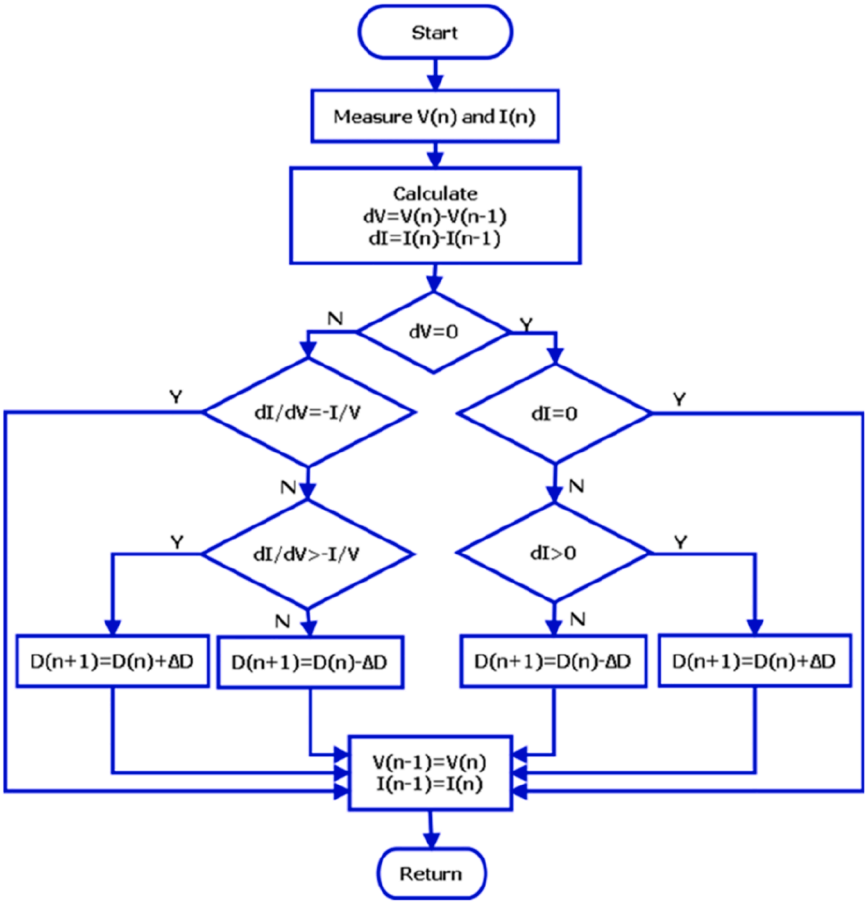

Fig. 2. Flowchart and algorithms of the incremental conductance method.

2.3. Measurement of operating conditions

We utilized a KIPP&ZONEN CMP11 pyranometer to measure irradiance, which provides a voltage signal ranging from 0 to 20 mV. The module backside temperature was monitored using a type K thermocouple, generating a voltage between 1 and 2.6 mV. The PV module current was measured using a shunt resistance of 0.01 Ω, resulting in a voltage drop between 0 and 3 mV. The PV module voltage was assessed using a voltage divider consisting of two precision resistors, 10 kΩ and 100 kΩ, with the PV voltage calculated from the voltage drop across the 10 kΩ resistance, ranging from 0 to 1.8 V. The voltage output of the sensors was captured using a 24-bit resolution ADC with an input impedance of 1 MΩ. Fig. 3(a) depicts exemplarily a time series measurement of the irradiance and module temperature.

Although data were collected around the clock, only records corresponding to daylight hours between 6:30 am and 5:30 pm were included for analysis. Additionally, average ambient conditions throughout the monitoring period included a yearly wind speed of 2.8 m/s, humidity below 40 %, and ambient temperatures between 17°C and 22°C.

Simultaneously, we measured the maximum power current and

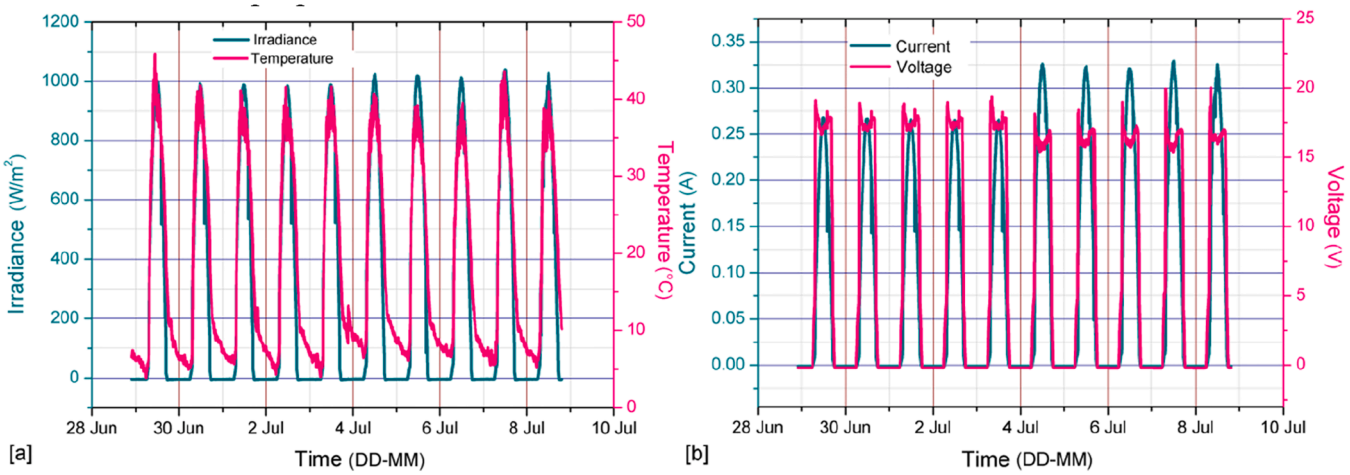

Fig. 3. (a) Measured irradiance and module temperature. (b) Measured current and voltage at maximum power. The PV module was cleaned on July 4.

voltage using the DC-DC converter, as illustrated in Fig. 3(b). The module was allowed to accumulate dust until July 4, after which it was cleaned. Fig. 3(b) depicts the subsequent increase in current. The data demonstrates that the proposed method, the hardware, and software facilitate the monitoring of dust's impact on maximum power. Subsequently, the data collected after July 4, when the module was free of dirt, was utilized to retrain the proposed models.

Fig. 3(b) illustrates a voltage drop of approximately 1 V following the module cleaning. Generally, the voltage at maximum power should remain relatively constant. The algorithm preserves maximum power even at the expense of a slight voltage drop, but a notable increase in current.

2.4. Electrical model of the photovoltaic module

In the data sheets, the majority of photovoltaic module manufacturers offer limited information on parameters contingent upon meteorological conditions such as irradiance and temperature. Consequently, we have made certain assumptions regarding the physical behavior of the cells in order to establish a model for the photovoltaic module. This section introduces a single-diode electrical model tailored for the 5 W monocrystalline module, which serves as a sensor for quantifying energy loss due to dust effects. Fig. 4 depicts the corresponding equivalent circuit. The module's characteristic I-V curve can be described by a nonlinear equation comprising multiple parameters, which can be categorized as follows: those provided by the manufacturer, those considered constants, and those necessitating calculation. Researchers have devised simplified methodologies in numerous studies where specific parameters cannot be directly determined.

Therefore, for simplicity, these parameters are assumed constant. For example, (Walker, 2001) includes a series resistor R_S in the model, but not the parallel resistor. The same assumption is made by (Benmessaoud et al., 2010; Kou et al., 1998) and (Chenni et al., 2007) consider a large parallel resistor. On the one hand, some authors disregard resistors in parallel and series; the former is because parallel resistance can be considered very large, and the latter because series resistance is usually minimal. On the other hand, other studies demonstrate that these two internal characteristics of PV modules are essential and should be determined more precisely, as shown in (Ishaque et al., 2011), depending also on the sky conditions (Sevillano-Bendezú et al., 2024). In addition to the series and parallel resistances, three other parameters must be determined; the photocurrent (I_{ph}), the saturation current (I_0), and the ideality factor (n) (Chouder et al., 2012; da Luz et al., 2018). The current–voltage relationship of a photovoltaic cell is given by:

$$I = I_{ph} - I_o\left[exp\left(\frac{V+IR_s}{A}\right)-1\right]-\frac{V+R_sI}{R_p} \tag{1}$$

where I_{ph} is the photocurrent in (A), I_o the diode saturation current (A), $A = nkT/q$ the modified ideality factor, n the diode ideality factor, k the Boltzmann constant (1.38×10^{-23}JK^{-1}), q the electronic charge (1.602×10^{-19}C), T the cell or module temperature (K), R_s the series resistance (Ω) and R_p is the shunt resistance (Ω). We use the data

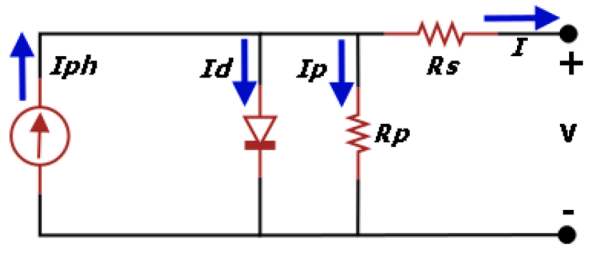

Fig. 4. Equivalent circuit of the single diode model with parallel and series resistances.

provided by the manufacturer in Table 1 and the model according to Eq. (1) to estimate this PV module's series and parallel resistance. Then we use the experimental data shown in Fig. 3(a) and (b) after cleaning the PV module to calibrate the model under real sun conditions. The calibration results are shown in Table 2. Using only the data provided by the manufacturer in Table 1 and the electrical model in Eq. (1), the error made in the power estimation is of the order of 10 %, as seen in Fig. 5(a). Calibrating the model under real sun conditions, we adjusted some parameters of the module so that the experimental generated power (P_g) and the estimated power (P_e) by the electrical model coincide, as shown in Fig. 5(b). After calibrating the model, the error in the power estimate is quantified according to the metrics shown in Table 4, for example, the mean absolute percentage error (MAPE) (Despotovic et al., 2015).

$$\boldsymbol{MAPE} = \frac{\sum_{i=1}^{m}\left|\left(\boldsymbol{P_g^i}-\boldsymbol{P_e^i}\right)/\boldsymbol{P_g^i}\right|}{\boldsymbol{m}}\times \mathbf{100\%} \tag{2}$$

Applying Eq. (2) to the data in Fig. 5(b) between 8 and 16 hours results in MAPE = 2.4 %.

2.5. Artificial Neural Network Model

The ANN model is composed of three input nodes, two hidden layers, and a single output layer. The network architecture is depicted in Fig. 6. The input vector $\boldsymbol{P^k} = (P_1^k, P_2^k, P_3^k) = (G^k, T^k, H^k)$ encompasses three variables: the irradiance G, the module temperature T, and the time H. The network's output a_1^3 provides an estimate of power, denoted as P_e. Each of the two hidden layers contains 14 neurons. The first layer's neurons each receive three inputs connected through synaptic weights $[W_{1,1}^1,\ W_{1,2}^1,\ \ldots..,\ W_{1,3}^1\ldots]$ and a trend input b_1^1, with superscripts denoting the layer and subscripts the neuron count within that layer.

The neuron's output is computed as $n_j^{k,1} = \mathbf{P}^k \bullet \mathbf{W}_j^1 + b_j^1$, where $\mathbf{n^1} = [n_1^{k,1}, n_2^{k,1}, \ldots, n_{14}^{k,1}]$ represents the net output subjected to an activation function f^1 to yield the neuron output $a_j^{k,1} = f^1\left(n_j^{k,1}\right)$, with $\mathbf{a^1} = [a_1^{k,1}, a_2^{k,1}, \ldots, a_{14}^{k,1}]$, where the super index indicates the layer and the sudindex indicates the neuron in the cape.

The inputs, outputs, synaptic weights, and trends of the neurons in each layer are expressible in matrix form (Sze et al., 2020). For instance, in Fig. 6, the 14 synaptic weights of the 14 neurons in layer 2 can be written as:

$$\boldsymbol{W^2} = \begin{bmatrix} \boldsymbol{W_{1,1}^2} & \boldsymbol{W_{1,2}^2} & \cdots & \boldsymbol{W_{1,14}^2} \\ \boldsymbol{W_{2,1}^2} & \boldsymbol{W_{2,1}^2} & \cdots & \boldsymbol{W_{2,14}^2} \\ \cdots & \cdots & \cdots & \cdots \\ \boldsymbol{W_{14,1}^2} & \boldsymbol{W_{14,1}^2} & \cdots & \boldsymbol{W_{14,14}^2} \end{bmatrix} \tag{3}$$

Table 2
Photovoltaic module electrical parameters after calibration at real sun conditions.

Electrical parameter	Symbol	Value
Maximum power	P_{mp}	5,7 W
Voltage at maximum power	V_{mp}	17,5 V
Current at maximum power	I_{mp}	0,33 A
Open-circuit voltage	V_{oc}	21,5 V
Current at maximum power	I_{sc}	0,36 A
Current temperature coefficient	μ_{sc}	$0{,}124\times 10^{-3}$ A/K
Voltage temperature coefficient	μ_{oc}	-2.9×10^{-3} V/K
Number of cells	N_s	36
Material band gap energy	ε_G	1,12 eV
Series resistance	R_s	2.00 Ω
Parallel resistance	R_P	1071 KΩ
Module area	area	0,0506 m^2
Fill factor	FF	0,761
Module efficiency	η	10,0

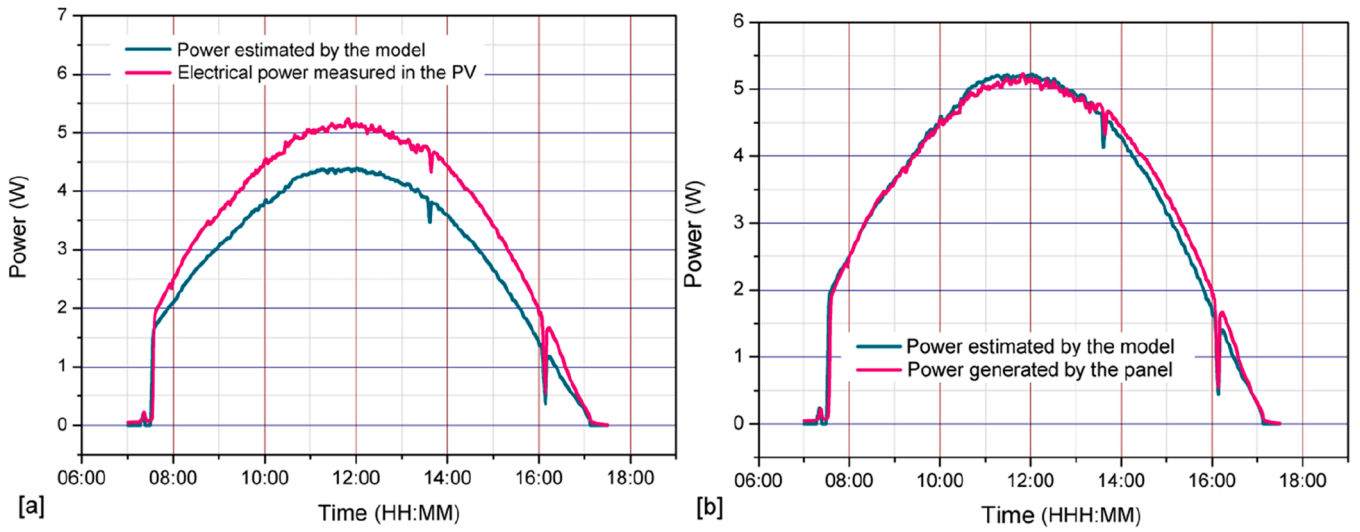

Fig. 5. Measured and modeled maximum power (electrical model) of test PV module (a) before and (b) after calibration at real sun conditions and after cleaning.

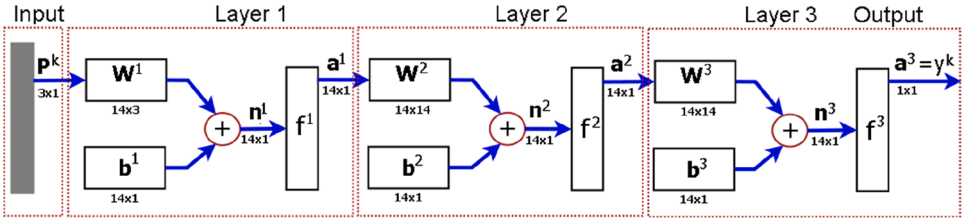

Fig. 6. Schematic of the three-layer ANN, shorthand notation.

Using matrix notation, we can write the output of each layer as shown below:

$$a^1 = f^1(W^1 \bullet P^k + b^1)$$

$$a^2 = f^2(W^2 \bullet a^{1,k} + b^2)$$

$$a^3 = f^3(W^3 \bullet a^{2,k} + b^3) \tag{4}$$

Finally, the output of the ANN can be written as:

$$Y_e^k = P_e^k = f^3(W^3 \bullet f^2(W^2 \bullet f^1(W^1 \bullet P^k + b^1) + b^2) + b^3) \tag{5}$$

The output of the trained network, when an input $P^k = [G^k, T^k, H^k]$ is presented, represents the electrical power P_e^k as given by Eq. (5). The selection of the activation function f^k is crucial and can significantly impact the model's accuracy and training time. In this work, we use the Gaussian Error Linear Unit (GELU) activation function, as proposed by (Hendrycks and Gimpel, 2016). The GELU function is a modification of the ReLU ("Rectified Linear Unit") function (Macêdo et al., 2019) and is defined as:

$$f^1(x) = f^2(x) = 0.5x\left(1 + tanh\left(\sqrt{2/\pi}\,(x + 0.044715x^3)\right)\right) \tag{6}$$

Compared to ReLU, GELU has the theoretical advantage of being differentiable for all values of x, but has the practical disadvantage of being much more computationally complex. The derivative of the GELU function is shown in Eq. (7).

$$\frac{df^1(x)}{dx} = 0.5 \bullet tanh(0,0356774x^3 + 0.797885x) + (0.053161x^3 + 0.398942x)\,\mathrm{sech}^2(0.0356774x^3 + 0.797885x) + 0.5 \tag{7}$$

We utilize the experimental data shown in Fig. 7(a) and (b), following the cleaning the PV module, to train the ANN model under real sunlight conditions. Fig. 7 illustrates the ANN training set, where the inputs H, G, and T are normalized, and the output is the generated power P_g. During the training process, an input $[H^k\ G^k\ T^k]$ and its corresponding output P_g^k are randomly selected, with k being the position or index of one of the training set examples. This example is propagated through the network according to Eq. (5) until the output generated power P_g^k or estimated power P_e^k is obtained.

Subsequently, we compute the error for example k with the Equation $e^k = \left(P_g^k - P_e^k\right)^2$, presenting all m examples of the training set in random order. The process of presenting the entire training set is known as an epoch, and the error incurred in a training epoch is calculated as the root mean square error defined as (Oh and Pyrczak, 2023)

$$e_{RSME} = \sqrt{\frac{1}{m}\sum_{i=1}^{m} e^i} \tag{8}$$

This error is employed to adjust the synaptic weights of the output layer and intermediate layers through a process known as back-propagation. The training set is presented to the network for the required number of epochs until the root mean square error reaches an acceptable level. The training algorithm, or optimizer, utilized in this

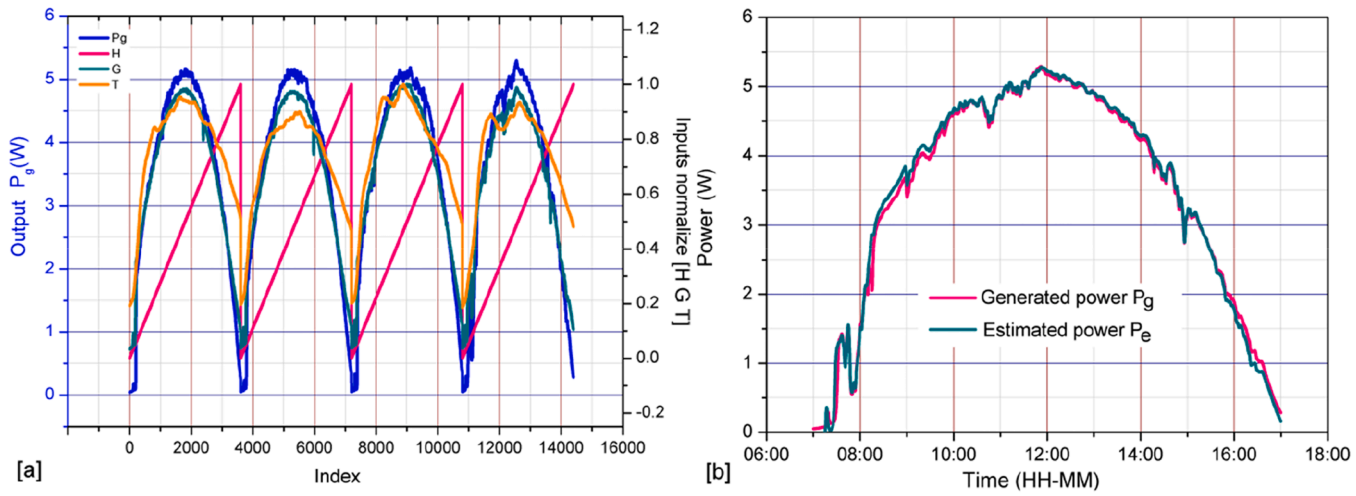

Fig. 7. Training set with normalized inputs after cleaning: time H, irradiance G, and module temperature T; and output generated power P_g. (b) Estimated (ANN-model) and measured power output P_e.

study is RMSprop (Tieleman et al., 2012), and the performance estimation metric employed is the MAPE Eq. (2).

The training set consists of 14,000 examples, and the weights in the ANN are readjusted every 128 examples per 150 training epochs. The predicted maximum power is shown in Fig. 7(b). The corresponding MAPE is calculated for the power output between 8 and 16 hours, resulting in a MAPE of 1.3 %. Conversely, for the electrical model utilizing the modeled maximum power depicted in Fig. 5(b), we obtain a MAPE of 2.4 %. For this exemplary day, the ANN model outperforms the electrical model in predicting the maximum power.

2.6. ANN architecture considerations

The training process is constrained to 150 epochs. It is imperative to select an ANN architecture that can effectively learn the training set depicted in Fig. 7(a).

To analyze the ANN's ability to learn and generalize from these training sets, we trained the ANN by varying the number of configurations (NC). In this case NC went up to 74, differing in the number of neurons in the hidden layers. Statistical metrics were employed to assess the performance of these architecture configurations, as presented in Table 3, where NC serves as an index for one of the 74 configurations.

The optimal configuration of the ANN can be identified by examining the statistics depicted in Fig. 8. The graph illustrates that the MAE, R^2, RMSE, and MAPE attain their optimal values when NC is approximately 20. Based on the notation in Table 3, we deduce that an ANN with 14 neurons in the hidden layers yields the most favorable outcomes.

These parameters were recorded under the following conditions: The solar module was cleaned on July 10 and allowed to accumulate dust for 24 days. Fig. 9(a) presents data from July 26 onward, with the module gathering dust until August 2, undergoing cleaning after 24 days. The

Table 3
Some of the statistics resulting from training 74 ANN configurations (NC).

NC	layer 1 neurons	layer 2 neurons	MAE	R^2
1	12	12	0.2615	0.9852
2	12	13	0.2646	0.9857
3	12	14	0.2644	0.9855
			:	:
19	13	19	0.1692	0.9921
20	14	14	0.1701	0.9935
21	14	15	0.1703	9.9922
			:	:
73	20	18	0.7157	0.9512
74	20	19	0.6542	0.9438

analytical models presented in previous sections utilized the post-cleaning data to estimate the maximum power output of a clean module. The module temperature reaches $45°C$ when the irradiance is around $1000W/m^2$, except on days 3 and 4 of August due to partially cloudy conditions. Occasionally, the irradiance exceeds $1100W/m^2$ due to cloud-enhancing effects. Based on this data, the model estimates the maximum power generated by the module under these conditions for each value of irradiance and temperature.

The recorded voltage and current at the maximum power point are depicted in Fig. 9(b). The current at maximum power, represented in black, is proportional to the irradiance and reaches 0.36 A when the irradiance is around $1000W/m^2$. The maximum power voltage in blue reaches 17 V when the irradiance is around $1000W/m^2$. The behavior of the maximum power voltage differs from that of the maximum power current. For instance, the current value peaks daily at $1000W/m^2$, whereas the maximum voltage is attained when the irradiance and temperature are lower. Cleaning has a negligible impact on the maximum power voltage; however, for the maximum power current, it is evident that from August 3 onwards, the maximum current increased by approximately 50 mA.

2.7. Calibration of models

In this sub-chapter, we describe the model calibration in more detail. The proposed device drives the PV module, which is used as a sensor, to work at maximum power. The measured power depends primarily on the module's received irradiance and cell temperature, as well as the soiling and degradation state. To account for the degradation effect on the soiling estimation, the models can be recalibrated after cleaning the module. At the time of cleaning, the data from the following days are used to recalibrate the models. This training and calibration data set is shown exemplarily in Fig. 10(a). The input data to the ANN are the irradiance G, the temperature T and the time of day H, the training algorithm must adjust the synaptic weights to produce the power given by $P = I_{mp} \bullet V_{mp}$, as described in the previous chapter.

To calibrate the electrical model, the proposed device operates as an $I-V$ curve transducer in reference conditions, ideally close to standard test conditions. Then, we use the referential electrical parameters of the $I-V$ and $P-V$ curves in Fig. 10(b), i.e., the short circuit current $I_{sc,ref}$, the open circuit voltage $V_{oc,ref}$, and the current $I_{mp,ref}$ and the voltage $V_{mp,ref}$ at maximum power point in the calibration procedure that will be described in detail as follows.

The PV module is composed of solar cells, with N_s representing the number of solar cells in series for the module. In this work, $N_s = 36$ for

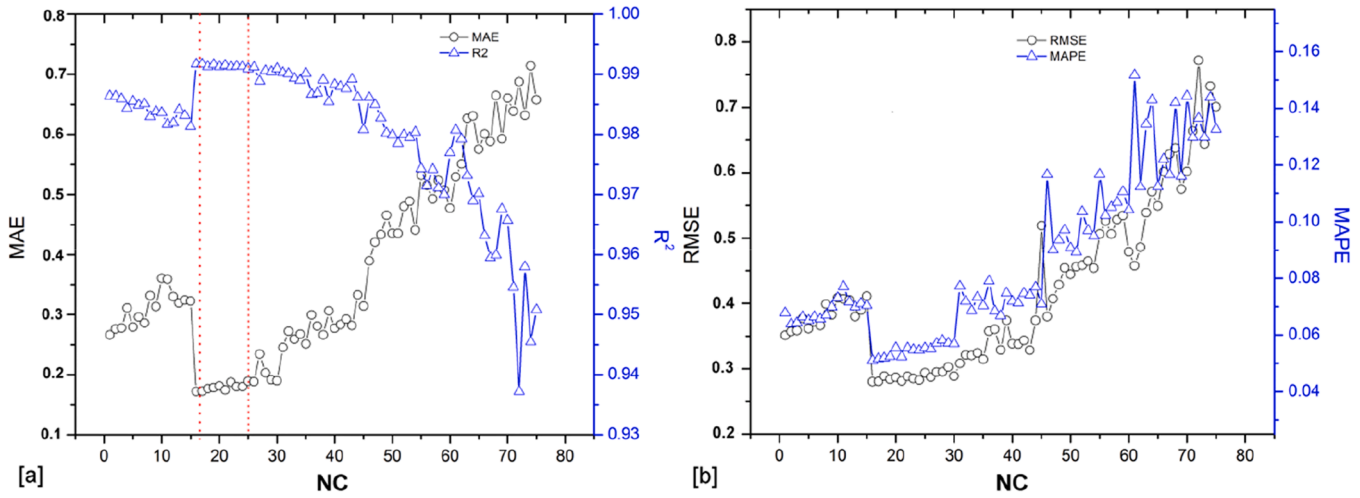

Fig. 8. (a) MAE, R^2, and (b) RMSE, MAPE for the 74 ANN configurations.

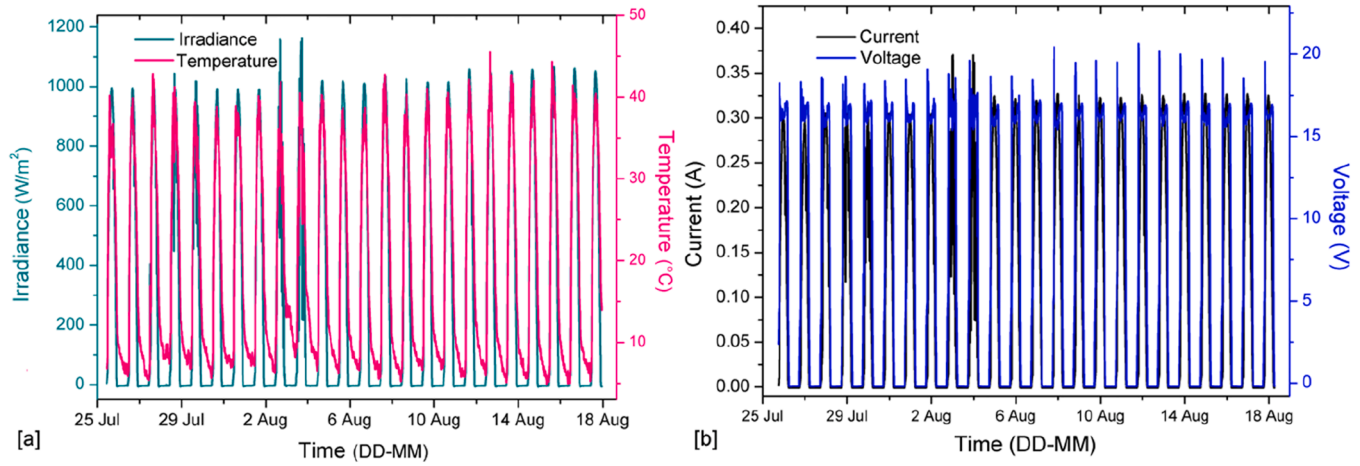

Fig. 9. (a) irradiance and module temperature, (b) Current and voltage, measured.

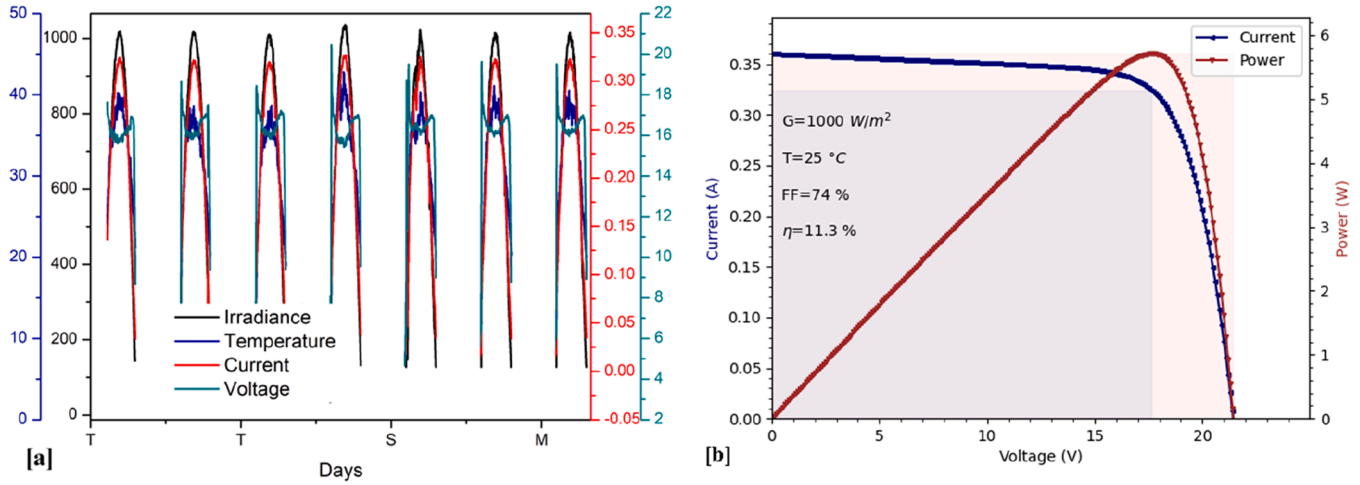

Fig. 10. Training dataset for the clean panel [a] running at maximum power and [b] as a tracer of I-V and P-V curves.

the module. When N_s solar cells are connected in series to form a module, the output current I and output voltage V of the module have the following relationship:

$$I = I_{ph} - I_o\left[\exp\left(\frac{q(V+IN_SR_S)}{N_snkT}\right)-1\right] - \frac{V+IN_SR_S}{N_SR_P} \quad (9)$$

The photocurrent I_{ph} depends on the solar irradiance G and the cell temperature T and is given by:

$$I_{ph} = \frac{G}{G_{ref}}\left[I_{ph,ref} + \mu_{sc}\left(T - T_{ref}\right)\right] \quad (10)$$

Here, μ_c is the short circuit current temperature coefficient of the module, $I_{ph,ref}$ is the reference photocurrent, and in each iteration, it can be recalculated as:

$$I_{ph,ref} = \frac{R_p + R_s}{R_p} I_{sc,ref} \quad (11)$$

The diode saturation current I_o is given by:

$$I_o = I_{o,ref}\left(\frac{T}{T_{ref}}\right)^3 \exp\left[\frac{q\cdot\varepsilon_G}{aK}\left(\frac{1}{T_{ref}} - \frac{1}{T}\right)\right] \quad (12)$$

Here, $I_{o,ref}$ is the nominal saturation current:

$$I_{o,ref} = \frac{I_{sc,ref} + \mu_{sc}\Delta T}{\exp\left[\left(V_{oc,ref} + \mu_{oc}\Delta T\right)/A\right] - 1} \quad (13)$$

with μ_{oc} as the open circuit temperature coefficient, and A is the modified ideality factor.

To calibrate the model, we first need to know the short circuit current, the open circuit voltage, and the maximum experimental power under reference conditions. The calibration procedure begins assuming that the series resistance $R_s = 0.0$, then we evaluate Eq. (9) under reference conditions. We clear and calculate R_p, with these resistance values, we calculate $I_{ph,ref}$ from Eq. (11) and I_{ph} from Eq. (10). From Eqs. (12) and (13), we calculate the reverse saturation current I_0. Finally, we use Eq. (9) to calculate m current values for m voltage values between 0 and V_{oc}. Fig. 11(a) depicts the resulting P-V curve, where we find the maximum power point and compare it with the experimental maximum power. If the estimated maximum power is greater than the experimental power, we increase the value of the series resistance $R_s = R_s + \Delta R_s$ and we repeat the procedure until the estimated maximum power is equal to the maximum experimental power. All the generated power curves are shown in Fig. 11(a). The maximum power point of each of these curves is graphed in Fig. 11(b) as a function of the resistance values; in each iteration, all the model parameters are recalculated.

Exemplarily, the P-V curves in Fig. 11(a), starting with a $R_s = 0.0\Omega$ and $R_p = 714.7\Omega$, are recalculated until the estimated power coincides with the experimental one of 5.7 W in Fig. 11(b), resulting in a series resistance $R_s = 2.0\Omega$ and a parallel resistance of $R_p = 1.071K\Omega$.

2.8. Coupling of physical quantities

In this study, we distinguish between two distinct phases: the calibration and training of the models, which occur either once or periodically depending on the degradation of the photovoltaic (PV) system used as a sensor, and the measurement and estimation of powers, which are conducted for each measured value of (t, G, T) and are related to the formulas as follows:

- The directly measured physical quantities include irradiance (G), module temperature (T), current at the maximum power point (I_{mp}), and voltage at the maximum power point (V_{mp}).
- The electrical power delivered by the module is calculated as $P_g = I_{mp} \times V_{mp}$ (W)
- In the electrical model, we estimate the module current using Eq. (1) $I_i = I_i\,(G, T)$ for n voltage values V_i in the modeled *I-V* curve between 0 and V_{OC}, in intervals of δV. Subsequently, we calculate the power $P_i = I_i \times V_i$ and plot the P-V curve. Then, the estimated power corresponds to the maximum power $P_e = P_{mp}$

Table 4
Statistical error metrics of power estimation for the clean PV module (Oh and Pyrczak, 2023).

Statistical error	Electrical model	ANN model
$MAE = \frac{1}{m}\sum_{i=1}^{m}\left\lvert P_g^i - P_e^i\right\rvert$ (W)	0.069	0.044
$RSME = \sqrt{\frac{1}{m}\sum_{i=1}^{m}\left\lvert P_g^i - P_e^i\right\rvert^2}$ (W)	0.116	0.090
$MAPE = \frac{\sum_{i=1}^{m}\left\lvert (P_g^i - P_e^i)/P_g^i\right\rvert}{m} \times 100\%$	2.5	1.5
$R^2 = \frac{\sum_{i=1}^{m}(P_g^i - \overline{P_g})(P_e^i - \overline{P_e})}{\sum_{i=1}^{m}\left(P_g^i - \overline{P_g}\right)^2 \sum_{i=1}^{m}\left(P_e^i - \overline{P_e}\right)^2}$	0.993	0.996

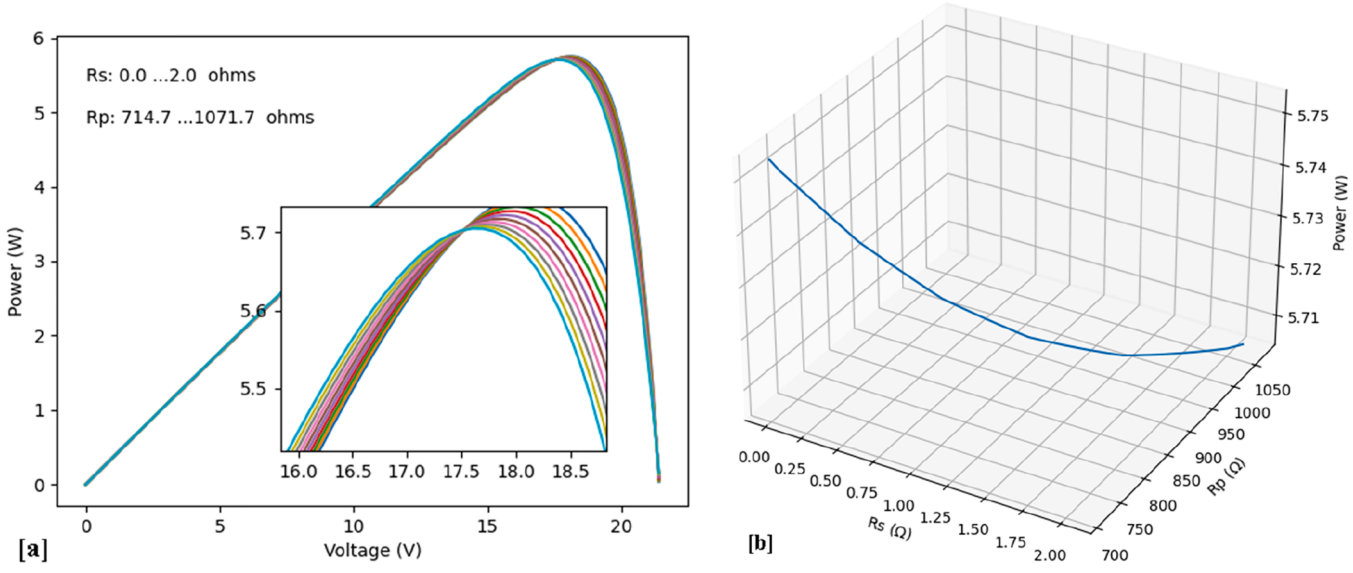

Fig. 11. Calibration of the electrical model if the maximum experimental power of the PV module under reference conditions is 5.7 W.

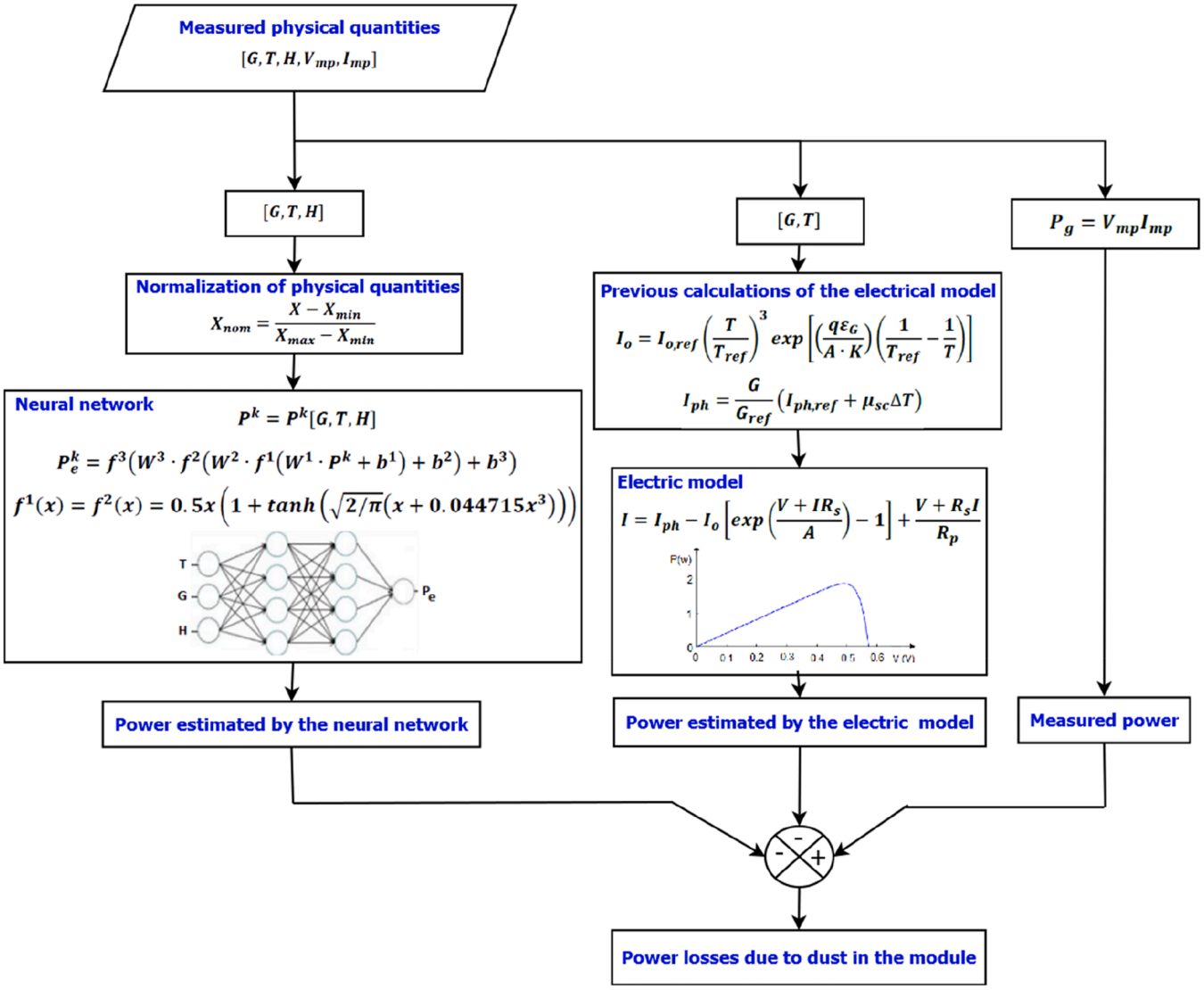

Fig. 12. Diagram depicting the coupling scheme of physical quantities for power loss estimation.

- In the ANN model, we estimate the power directly from Eq. (5) $P = P(t, G, T)$.
- We employ statistical metrics outlined in Table 4 to assess the precision of the estimation.

The diagram in Fig. 12 summarizes the measurement and calculation procedures performed by the system once the neural network has been trained and the electrical model calibrated. It begins by measuring the physical quantities irradiance G, module temperature T, time H, voltage V_{mp}, and current I_{mp} at the MPP. The ANN estimates the maximum power from the normalized values (between 0 and 1). The electrical model estimates the power based on irradiance and module temperature. The measured V_{mp} and current I_{mp} yield the maximum power; finally, subtract the estimated power from the measured power and identify this value as a loss of power performance due to module soiling.

3. Results and discussion

3.1. The models' accuracy in power estimation for a clean PV module

The first monthly set of experimental data (G, T, I_{mp}, V_{mp}) is used to estimate the precision of the models in estimating the PV module's power under clean conditions with a daily cleaning schedule to minimize any impact from soiling. This month's data consists of 4000 samples per day. Half of this month's data, randomly selected, is allocated for calibrating the electrical model and training the ANN, while the other half is reserved for testing the models' power estimation capabilities. The methodology adopted is illustrated in Fig. 13(a) for the electrical model and (b) for the ANN for an exemplary day. At the top, the graphs depict the measured power (Pattern) and the power estimated by the models (Test) as a function of time. Notably, there is a slight decline in prediction accuracy when abrupt changes in irradiance occur. This is due to the MPPT setup employed, which includes a DC-DC converter and the incremental conductance algorithm, lacking the agility to adjust to swift irradiance fluctuations promptly. This limitation of the MPPT algorithm has been emphasized in numerous studies. To mitigate this issue, the search for the maximum power point could be limited to a specific voltage range where the maximum power point is anticipated based on irradiance and temperature data. This method, known as hybrid algorithms, has been extensively reviewed by (Krithiga et al., 2023).

In the middle section of Fig. 13, the measured power is plotted against the estimated power, demonstrating their linear relation. The lower part displays a histogram of the residuals. The histogram of residuals, shown in Fig. 13, exhibits a normal distribution, corroborated by the Durbin-Watson test, indicating that the errors are random in

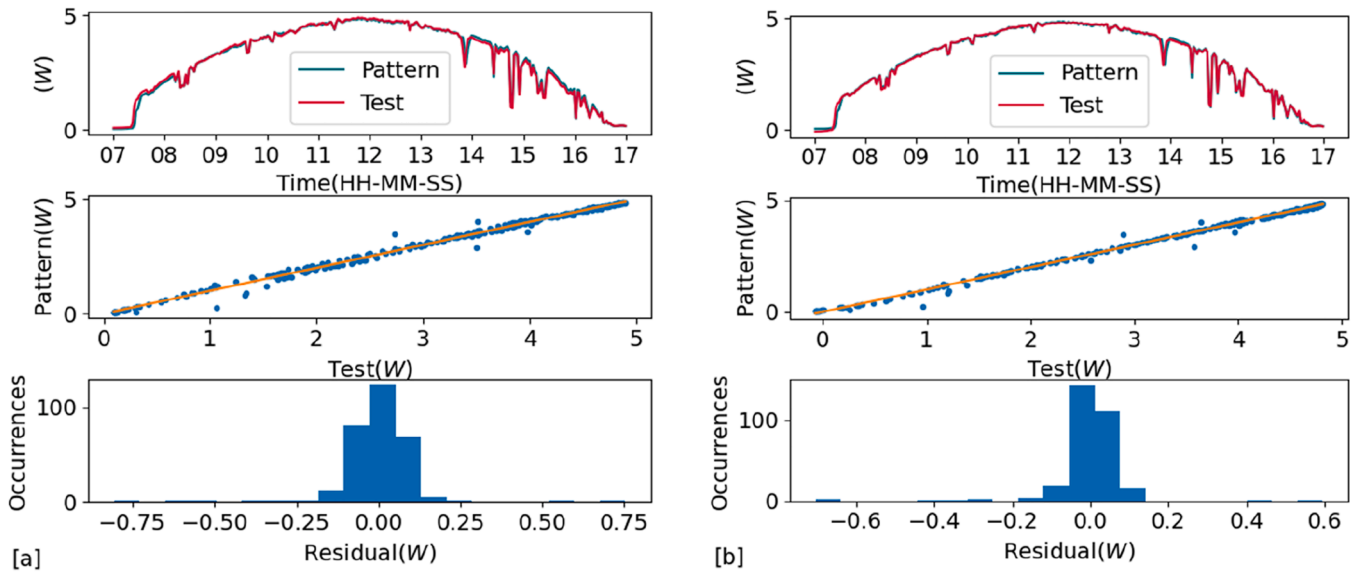

Fig. 13. Example to determine the precision of power estimates, where the pattern is the measured power and test is the estimated power by (a) the electric model and (b) the ANN model.

nature.

A summary of the error statistics for the entire month's test set is provided in Table 4. The statistical analysis reveals the superiority of the ANN model over the electrical model, as it yields lower errors for all four metrics. However, this assertion should be approached with caution. In solving the electrical model, Eq. (1) must be solved iteratively for voltage values ranging from 0 V to V_{OC}. The accuracy with which the maximum power point can be estimated with the electrical model, as well as the computational cost of the model, is determined by the number of intervals into which the voltage range is divided. In conclusion, while it is possible to enhance the performance of the electrical model to estimate power losses, this improvement comes at the expense of increased computational resources.

When the PV module is clean or devoid of dust, the statistics outlined in Table 4 are pertinent. These results demonstrate that the models'

Table 5
Statistical error metrics of energy estimation for the clean PV module.

Statistical error	Electrical model	ANN model
$MAE = \frac{1}{m}\sum_{i=1}^{m}\left\lvert E_g^i - E_e^i\right\rvert$ (Wh)	0.205	0.174
$RSME = \sqrt{\frac{1}{m}\sum_{i=1}^{m}\left\lvert E_g^i - E_e^i\right\rvert^2}$ (Wh)	0.235	0.210
$MAPE = \frac{\sum_{i=1}^{m}\left\lvert (E_g^i - E_e^i)/E_g^i\right\rvert}{m} \times 100\%$	0.60	0.50
$R^2 = \frac{\sum_{i=1}^{m}(E_g^i - \overline{E_g})(E_e^i - \overline{E_e})}{\sum_{i=1}^{m}\left(E_g^i - \overline{E_g}\right)^2 \sum_{i=1}^{m}\left(E_e^i - \overline{E_e}\right)^2}$	0.992	0.993

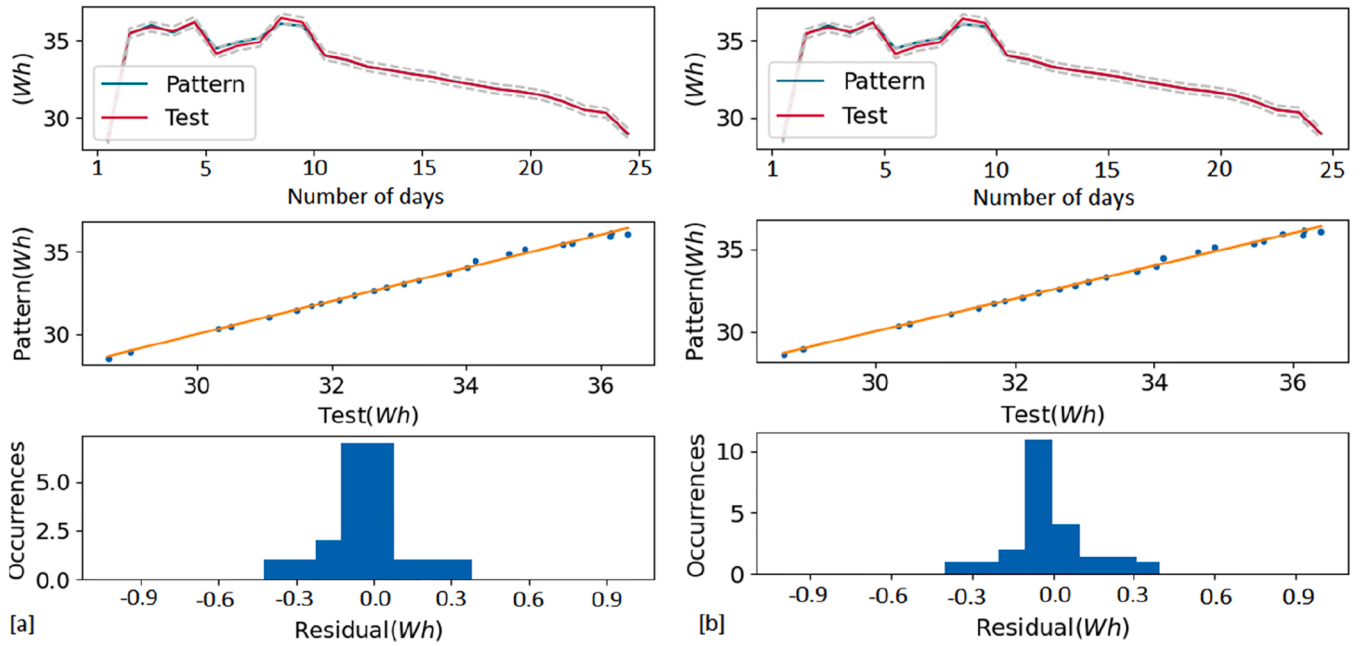

Fig. 14. Estimation of daily energy with (a) the electrical model and (b) the ANN model.

accuracy in estimating power output is approximately 2 % over a data collection span of one year.

3.2. The models' accuracy in energy estimation for a clean PV module

We maintain the photovoltaic module used as a sensor clean and free of dust for 25 days to quantify the error of the models in estimating the generated energy. The daily harvested energy is measured and compared to estimates obtained using the electrical model in Fig. 14(a) and the ANN model in Fig. 14(b). The resulting statistical errors are summarized in Table 5. During the 25 days, the daily energy ranged between 25 and 36 Wh due to variations in irradiation and temperature. The results indicate that the models predict the energy with a mean absolute percentage error (MAPE) of 0.6 % and 0.5 % for the electrical and ANN models, respectively.

3.3. Computational costs

Upon calibrating the electrical model and training the neural network model, they can be utilized to predict daily energy output. The corresponding computational costs for each method are estimated as follows:

- Utilizing the exemplary daily dataset depicted in Fig. 15(a) the electrical model employs iterative techniques to solve Eq. 9 for each pair of irradiance and temperature. For this process, $P_{i,j} = P_i(G_j,\ T_j,\ V_i)$ is computed where V_i ranges from 0 V to V_{oc} in increments of $\delta_V = 0.5$V. Subsequently, the j^{th} curve $P_{i,j} - V_i$ is plotted for $0 < i < 43$ for a module with $V_{oc} = 21.5$V. From the $P-V$ curve we estimate $P_{i,j\max}$ and repeat this for all the experimental values of G_j, T_j where $0 < j < 4000$, as shown in Fig. 15(b). The number of times that Eq. (9) is solved is equal to the number of experimental data (G_j,T_j,) multiplied by V_{oc}/δ_V, resulting in approximately $(4000 \times 21.5)/0.5 = 172000$ solutions. Using the electrical model for estimating the energy loss due to soiling yields a corresponding computational cost expressed in seconds of 35.430 s per daily dataset.
- For the neural network model, which consists of three inputs, two layers with 14 units each, and a fully connected output unit, the input signal is processed according to Eq. (5) for each experimental point (G_j,T_j,t_j) depicted in Fig. 15[a]. The Equation for the ANN model is solved for each data point in the dataset, with the computational time being 0.087 s per daily dataset.

The computational cost of solving the electrical model is much higher than that of the artificial neural network. This discrepancy arises from both the greater number of operations required and the complexity of these operations. Specifically, in the electrical model, Eq. (9) requires the use of iterative methods to derive its solution.

3.4. Energy loss estimation due to soiling

Following the calibration and training of both models and quantifying their error in power estimation for a clean module, we used another month of data to compare the estimated power to the measured power, this time with the module subjected to soiling and one cleaning.

By integrating the daily power curves estimated by both models and the power curve measured from the PV module, we obtained the corresponding daily energies shown in Fig. 16(a). The daily energies estimated by the electrical model (EM) and the ANN are remarkably consistent. The module was allowed to accumulate dust for 24 days until August 2, when we cleaned it. Up to this point, there was a discrepancy between the energies estimated by the models and the measured ones caused by the impact of soiling. The estimated and measured energy values coincided after cleaning the PV module on August 2. Subsequently, the discrepancy increased again due to continuous soiling. The impact of soiling and cleaning is also clearly visible in Fig. 16(b), which shows the clean PV module's estimated efficiency compared to the soiled module's measured efficiency. The efficiency of the clean PV module is about 10.2 %, which falls to 9.6 % due to dust accumulation.

To estimate the daily or monthly energy losses (E_p) due to soiling, we subtracted the measured energy generated by the PV module from the energy estimated by the electrical and ANN models. Fig. 17[a] shows the daily losses calculated from the same data as in Fig. 16. Before cleaning the module, the energy loss estimated by both models is around 5 % over the 24 days of dust accumulation. After cleaning the module on August 2, both models show the same behavior: energy losses increase as dust accumulates again on the module.

In general, the increasing tendency for energy loss is as expected. However, the losses also fluctuate from day to day, which can be attributed to two factors. In the first place, the dust or dirt settling on the module can decrease due to wind effects. This depends on the nature of the dust or dirt. In some cases, the dust adheres strongly to the surface; in others, it does not. In this effect of adherence, relative humidity plays an important role. Secondly, the aerosols suspended in the atmosphere block and modify the solar spectrum. Due to its limited spectral response, the module's current is sensitive to changes in the solar spectrum, whereas the pyranometer has a much broader and flat spectral response and is much less sensitive.

Finally, Fig. 17[b] demonstrates the monthly energy losses due to soiling during an entire year from 2020 to 09–01 to 2021–09–01. During this year, the PV module was cleaned every 24–30 days, approximately once per month. As shown, both models give similar loss results. During

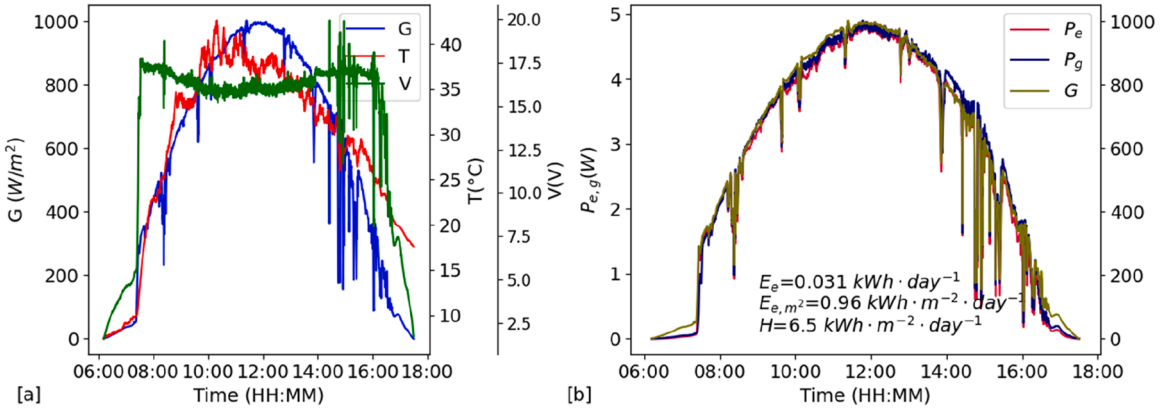

Fig. 15. (a) Exemplary daily data set of irradiance G, module temperature T, and voltage V of the PV module. (b) Power $\boldsymbol{P_e}$ estimated by the models, power $\boldsymbol{P_g}$ generated by the module and irradiance for the same day. $\boldsymbol{E_e}$, $\boldsymbol{E_{e,m^2}}$, and $\boldsymbol{H}$ are the estimated daily energy using the ANN, the estimated daily energy per $\boldsymbol{m^2}$ and the daily irradiation, respectively.

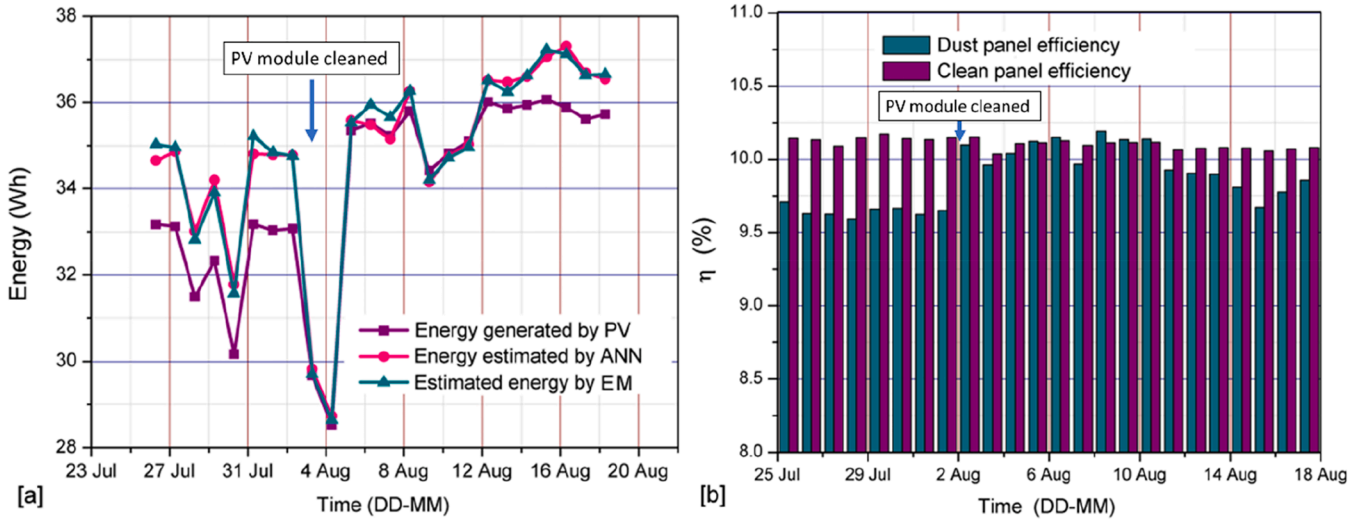

Fig. 16. (a) Measured and estimated energy generated by the PV module. (b) Measured efficiency of the PV module with dust accumulation compared with estimated efficiency under clean conditions using the ANN model.

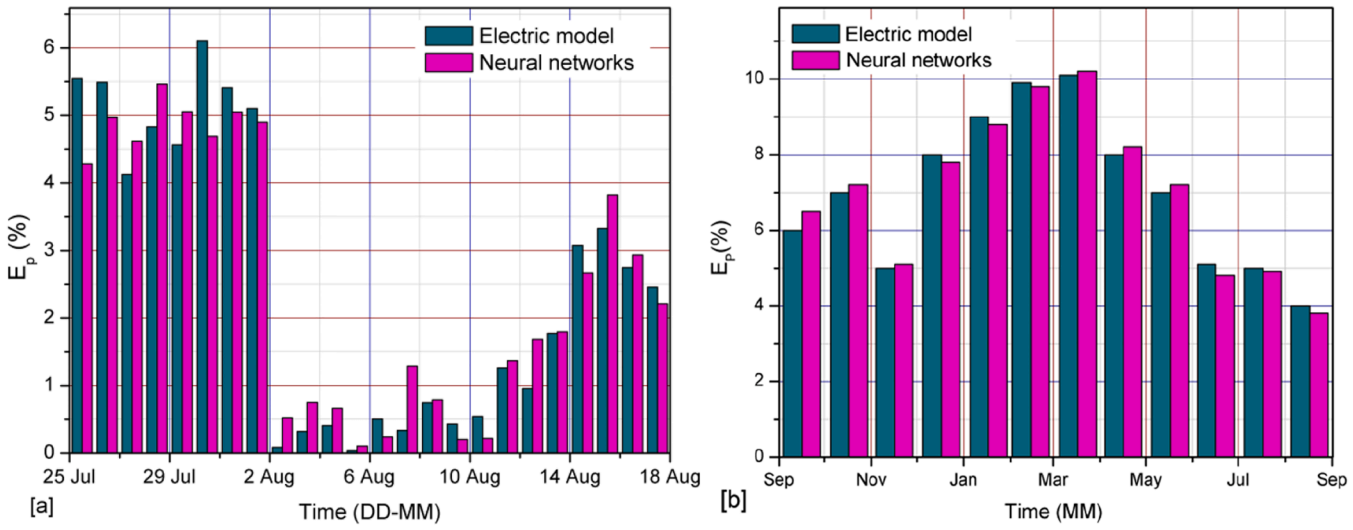

Fig. 17. Comparison of energy lost, (a) daily and (b) monthly, estimated with both models.

most months, the losses oscillate between 4 % and 7 %. However, between December and April, we observed elevated losses of up to 10 % due to soiling. This increase was caused by nearby construction activities generating more dust.

3.5. Additional considerations

The system introduced in this study does not require additional inputs or mechanisms for its operation. Moreover, the energy needed to power the system can be sourced from photovoltaic means, and it does not necessitate a distinct cleaning regimen. The cleaning schedule can be synchronized with the maintenance cycle of the PV plant where it is implemented to measure dust losses. This system offers the advantage of immediate deployment, with daily updates on performance loss data. The only regular maintenance the system requires is cleaning the pyranometer dome from dust, which is minimal.

Furthermore, the system is modular and can be adapted to site-specific conditions. For instance, since dust distribution and soiling losses can be affected by PV module size and glass surface type, the system's PV module can be replaced with one of the plant's own modules when deployed in the field. Additionally, the system's power electronics can be adjusted to accommodate the new PV module's power specifications. Consequently, this adaptability allows the system to provide even more accurate estimations of the PV plant's energy losses due to soiling.

As for the technology used in the sensor module, the mini-module implemented in the system is made of monocrystalline silicon technology based on Back Surface Field (BSF) solar cells. Therefore, it can be assumed that the estimated losses with this mini-module should be close to possible losses by a PV system of similar monocrystalline silicon-based technologies, such as Passivated Emitter and Rear Cells (PERC), Tunnel Oxide Passivated Contact (TOPcon), and Heterojunction Technology (HJT). In principle, this system can be adapted to a module of the same technology implemented in a PV plant that is to be installed, which gives it flexibility of adaptation.

However, there are two limitations that must be considered in the practical application of this system.

The first is the degradation of the photovoltaic module. The enduring accuracy of the system hinges on the models' abilities to estimate power accurately; however, these models do not account for the degradation parameters of the PV module when used as a sensor. Despite the PV module being made of monocrystalline cells, which are renowned for

their stability, literature has documented an average degradation rate of about 1 % per year (Jordan and Kurtz, 2013). The system offers the advantage of performing a recalibration of the electrical model or retraining the ANN under clean PV module conditions to compensate for any long-term degradation. A recalibration of the PV module after the 1-year measurement yielded negligible differences in the electrical parameters shown in Table 2, as obtained at the initiation of the experiment, demonstrating a degradation < 1 % in its maximum power. An analysis of the system's long-term stability above one year is currently being conducted, but it is out of the scope of this work. Implementing an automatic recalibration process could be a better solution, which only requires software updates.

The second limiting factor that must be considered is the soiling of the pyranometer. Although the pyranometer used in this work is a double semi-spherical dome that is self-cleaning to a certain extent, dirt or dust on the surface of the pyranometer dome cannot be ignored. As performed in this study, the pyranometer requires regular cleaning to minimize the impact of dust accumulation on the dome.

4. Conclusions

In this study, we introduced a novel, self-contained, portable system for estimating soiling losses in PV modules. Our system and methodology, termed Incremental Neuroconductance, measures a PV module's power subjected to soiling using MPPT based on the incremental conductance method and compares it to the estimated power of a clean module using ANN and electrical models based on irradiance and module temperature measurements. The system facilitates both pre-implementation and operational on-site soiling analysis of PV systems, accounting for spatial inhomogeneities of dust accumulation and the long-term degradation of PV modules through recalibration and retraining.

We conducted a detailed evaluation and comparison between the electrical and ANN models. Both models exhibited comparable performances in estimating a clean PV module's energy output, with the ANN model demonstrating lower computational costs. The ANN model also showed slightly better accuracy, with a MAPE of 0.5 % compared to 0.6 % for the electrical model. These results indicate that while both models are effective, the ANN model offers advantages in terms of computational efficiency and adaptability for retraining to compensate for long-term module degradation.

Based on a one-year test period in the desertic region of Arequipa, Peru, our findings demonstrate the system's capability to accurately predict performance losses due to soiling without the need for a complete PV system setup. The results showed that, when employing a monthly cleaning schedule, the energy losses due to soiling oscillated between 4 % and 7 % during most months, with elevated losses of up to 10 % observed in months with nearby construction activities and a yearly loss of about 7 %, with an error of 0.5 % for the ANN and 0.6 % for the electrical model.

The system's adaptability allows it to be tailored to site-specific conditions, such as replacing the PV module with one of the plant's own modules and adjusting the system's power electronics to match the new module's power specifications. This modularity enhances the accuracy of soiling loss estimations for specific PV plants.

Developing optimal cleaning schedules and enhancing plant bankability are essential priorities for stakeholders in the photovoltaic sector when planning large-scale installations in desert regions. The Incremental Neuroconductance system presents a robust and flexible solution for quantifying soiling losses in PV modules, contributing to more effective maintenance schedules and improved PV plant performance. Future work will focus on extending the long-term stability analysis of the system beyond one year and exploring additional applications in various climatic regions.

CRediT authorship contribution statement

Ernesto Palo-Tejada: Writing – review & editing, Writing – original draft, Software, Methodology, Conceptualization. **Victoria Campos-Falcon:** Writing – review & editing, Writing – original draft, Visualization, Data curation. **Jan Amaru Töfflinger:** Writing – review & editing, Validation.

Declaration of Competing Interest

The authors declare that they have no known competing financial interests or personal relationships that could have appeared to influence the work reported in this paper.

Acknowledgments

The authors thank the National University of San Agustín de Arequipa for financing the basic and applied research project "Concentration gradients of particulate matter in surface mining use neural networks, low-cost optoelectronic sensors, and unmanned aerial vehicles" with contract number IAI-003–2018-UNSA. J. A. Töfflinger acknowledges the financial support from PROCIENCIA through contract PE501078395–2022 and from the Vicechancellorship for Research of the Pontificia Universidad Católica del Perú through contract number 2023-F-0023-PI0997.

Data availability

Data will be made available on request.

References

Abraim, M., El Ydrissi, M., Ghennioui, H., Ghennioui, A., Hanrieder, N., Wilbert, S., Azouzoute, A., 2023. PVSMS: a system for quantifying soiling effects and optimizing cleaning schedule in PV solar plants. Energy Convers. Manag. 284, 116978.

Adothu, B, Kumar, S, John, JJ, et al., 2024. Comprehensive review on performance, reliability, and roadmap of c-Si PV modules in desert climates: A proposal for improved testing standard. Prog Photovolt Res Appl 32 (8), 495–527.

Almasoud, A.H., Gandayh, H.M., 2015. Future of solar energy in Saudi Arabia. J. King Saud. Univ. -Eng. Sci. 27, 153–157.

Alnaser, N.W., Dakhel, A.A., Al Othman, M.J., Batarseh, I., Lee, J.K., Najmaii, S., Alnaser, W.E., 2015. Dust accumulation study on the Bapco 0.5 MWp PV project at University of Bahrain. Int. J. Power Renew. Energy Syst. 2, 53.

Beattie, N.S., Moir, R.S., Chacko, C., Buffoni, G., Roberts, S.H., Pearsall, N.M., 2012. Understanding the effects of sand and dust accumulation on photovoltaic modules. Renew. Energy 48, 448–452.

Benghanem, M., Almohammedi, A., Khan, M.T., Al-Masraqi, A., 2018. Effect of dust accumulation on the performance of photovoltaic panels in desert countries: A case study for Madinah, Saudi Arabia. Int. J. Power Electron. Drive Syst. 9, 1356.

Benmessaoud, M.T., Zerhouni, F.Z., Zegrar, M., Stambouli, A.B., Tioursi, M., 2010. New approach modeling and a maximum power point tracker method for solar cells. Comput. Math. Appl. 60, 1124–1134.

Caron, J.R., Littmann, B., 2012. Direct monitoring of energy lost due to soiling on first solar modules in California. IEEE J. Photovolt. 3, 336–340.

Chanchangi, Y.N., Roy, A., Ghosh, A., Sundaram, S., Mallick, T.K., 2021. In-situ assessment of photovoltaic soiling mitigation techniques in northern Nigeria. Energy Convers. Manag. 244, 114442.

Chatterjee, S, Das, A, 2023. A review on technological aspects of different PWM techniques and its comparison based on different performance parameters. Int J Circ Theor Appl 51 (5), 2446–2498.

Chenni, R., Makhlouf, M., Kerbache, T., Bouzid, A., 2007. A detailed modeling method for photovoltaic cells. Energy 32, 1724–1730.

Chouder, A., Silvestre, S., Sadaoui, N., Rahmani, L., 2012. Modeling and simulation of a grid connected PV system based on the evaluation of main PV module parameters. Simul. Model. Pract. Theory 20, 46–58.

Cordero, R.R., Damiani, A., Laroze, D., Macdonell, S., Jorquera, J., Sepúlveda, E., et al., 2018. Effects of soiling on photovoltaic (PV) modules in the Atacama Desert. Sci. Rep. 8, 13943.

Daliento, S., Di Napoli, F., Guerriero, P., d'Alessandro, V., 2016. A modified bypass circuit for improved hot spot reliability of solar panels subject to partial shading. Sol. Energy 134, 211–218.

Dehshiri, S.S., Firoozabadi, B., 2023. Dust cycle, soiling effect and optimum cleaning schedule for PV modules in Iran: A long-term multi-criteria analysis. Energy Convers. Manag. 286, 117084.

Deng, S., Zhang, Z., Ju, C., Dong, J., Xia, Z., Yan, X., Xing, G., 2017. Research on hot spot risk for high-efficiency solar module. Energy Procedia 130, 77–86.

Despotovic, M., Nedic, V., Despotovic, D., Cvetanovic, S., 2015. Review and statistical analysis of different global solar radiation sunshine models. Renewable and Sustainable Energy Reviews 52, 1869–1880.
Escobar Moragas, R., Cortés, C., Pino, A., Salgado, M., Pereira, E.B., Ramos Martins, F., Cardemil, J.M., 2015. Estimating the potential for solar energy utilization in Chile by satellite-derived data and ground station measurements. Sol. Energy 121, 139–151.
Fan, S., Wang, Y., Cao, S., Sun, T., Liu, P., 2021. A novel method for analyzing the effect of dust accumulation on energy efficiency loss in photovoltaic (PV) system. Energy 234, 121112.
Gostein, M., Düster, T., & Thuman, C. (2015). Accurately measuring PV soiling losses with soiling station employing module power measurements. *2015 IEEE 42nd Photovoltaic Specialist Conference (PVSC)*, (pp. 1–4).
Gude, S., Jana, K.C., Laudani, A., Thanikanti, S.B., 2022. Parameter extraction of photovoltaic cell based on a multi-objective approach using nondominated sorting cuckoo search optimization. Sol. Energy 239, 359–374.
Hanifi, H., Schneider, J., & Bagdahn, J. (2015). Reduced shading effect on half-cell modules—Measurement and simulation. 2529–2533.
Hegazy, A.A., 2001. Effect of dust accumulation on solar transmittance through glass covers of plate-type collectors. Renew. Energy 22, 525–540.
Hendrycks, D., & Gimpel, K. (2016). Gaussian error linear units (gelus). *arXiv preprint arXiv:1606.08415*.
Igathinathane, C., Melin, S., Sokhansanj, S., Bi, X., Lim, C.J., Pordesimo, L.O., Columbus, E.P., 2009. Machine vision based particle size and size distribution determination of airborne dust particles of wood and bark pellets. Powder Technol. 196, 202–212.
Ilse, K., Figgis, B., Khan, M.Z., Naumann, V., Hagendorf, C., 2018b. Dew as a detrimental influencing factor for soiling of PV modules. IEEE J. Photovolt. 9, 287–294.
Ilse, K.K., Figgis, B.W., Naumann, V., Hagendorf, C., Bagdahn, J., 2018a. Fundamentals of soiling processes on photovoltaic modules. Renew. Sustain. Energy Rev. 98, 239–254.
Ilse, K., Micheli, L., Figgis, B.W., Lange, K., Daßler, D., Hanifi, H., et al., 2019. Techno-economic assessment of soiling losses and mitigation strategies for solar power generation. Joule 3, 2303–2321.
Ishaque, K., Salam, Z., et al., 2011. A comprehensive MATLAB Simulink PV system simulator with partial shading capability based on two-diode model. Sol. Energy 85, 2217–2227.
Jathar, L.D., Ganesan, S., Awasarmol, U., Nikam, K., Shahapurkar, K., Soudagar, M.E., et al., 2023. Comprehensive review of environmental factors influencing the performance of photovoltaic panels: Concern over emissions at various phases throughout the lifecycle. Environ. Pollut., 121474
Javed, W., Guo, B., Figgis, B., Pomares, L.M., Aïssa, B., 2020. Multi-year field assessment of seasonal variability of photovoltaic soiling and environmental factors in a desert environment. Sol. Energy 211, 1392–1402.
Jiang, H., Lu, L., Sun, K., 2011. Experimental investigation of the impact of airborne dust deposition on the performance of solar photovoltaic (PV) modules. Atmos. Environ. 45, 4299–4304.
Jordan, D.C., Kurtz, S.R., 2013. Photovoltaic degradation rates—an analytical review. Progress in photovoltaics: Research and Applications 21 (1), 12–29.
Kaldellis, J.K., Kapsali, M., 2011. Simulating the dust effect on the energy performance of photovoltaic generators based on experimental measurements. Energy 36, 5154–5161.
Karami, N., Moubayed, N., Outbib, R., 2017. General review and classification of different MPPT Techniques. Renew. Sustain. Energy Rev. 68, 1–18.
Kim, E., Warner, M., & Bhattacharya, I. (2020). Adaptive step size incremental conductance based maximum power point tracking (mppt). *2020 47th IEEE Photovoltaic Specialists Conference (PVSC)*, (pp. 2335–2339).
Kimber, A., Mitchell, L., Nogradi, S., & Wenger, H. (2006). The effect of soiling on large grid-connected photovoltaic systems in California and the southwest region of the United States. *2006 IEEE 4th World Conference on Photovoltaic Energy Conference, 2*, pp. 2391–2395.
Koirala, B.P., Sahan, B., & Henze, N. (2009). Study on MPP mismatch losses in photovoltaic applications. *European Photovoltaic Solar Energy Conference and Exhibition (EU PVSEC)*, (pp. 3727–3733).
Korevaar, M., Mes, J., Nepal, P., Snijders, G., & van Mechelen, X. (2017). Novel soiling detection system for solar panels. *33rd European Photovoltaic Solar Energy Conference and Exhibition*, (pp. 2349–2351).
Kou, Q., Klein, S.A., Beckman, W.A., 1998. A method for estimating the performance of photovoltaic systems. Sol. Energy 64, 33–40.
Krithiga, G., Mohan, V., Chitrakala, G., Senthilkumar, S., 2023. OPTIMIZATION OF SWITCHING ANGLES FOR SELECTIVE HARMONIC ELIMINATION IN CASCADED H-BRIDGE MULTILEVEL INVERTERS EMPLOYING ARTIFICIAL INTELLIGENCE TECHNIQUES–A MINI REVIEW. Int. J. Eng. Technol. Manag. Res. 10, 1–16.
Luque, E.G., Antonanzas-Torres, F., Escobar, R., 2018. Effect of soiling in bifacial PV modules and cleaning schedule optimization. Energy Convers. Manag. 174, 615–625.
da Luz, C.M., Tofoli, F.L., dos Santos Vicente, P., Vicente, E.M., 2018. Assessment of the ideality factor on the performance of photovoltaic modules. Energy Convers. Manag. 167, 63–69.
Macêdo, D., Zanchettin, C., Oliveira, A.L., Ludermir, T., 2019. Enhancing batch normalized convolutional networks using displaced rectifier linear units: A systematic comparative study. Expert Syst. Appl. 124, 271–281.
Maghami, M.R., Hizam, H., Gomes, C., Radzi, M.A., Rezadad, M.I., Hajighorbani, S., 2016. Power loss due to soiling on solar panel: A review. Renew. Sustain. Energy Rev. 59, 1307–1316.
Muller, M., Micheli, L., Solas, A.F., Gostein, M., Robinson, J., Morely, K., et al., 2021. An in-depth field validation of "DUSST": a novel low-maintenance soiling measurement device. Prog. Photovolt.: Res. Appl. 29, 953–967.
Obukhov, S., Ibrahim, A., Diab, A.A., Al-Sumaiti, A.S., Aboelsaud, R., 2020. Optimal performance of dynamic particle swarm optimization based maximum power trackers for stand-alone PV system under partial shading conditions. IEEE Access 8, 20770–20785.
Oh, D.M., Pyrczak, F., 2023. Making sense of statistics: A conceptual overview. Routledge.
Olivares, D., Ferrada, P., Bijman, J., Rodríguez, S., Trigo-González, M., Marzo, A., Fuentealba, E., 2020. Determination of the soiling impact on photovoltaic modules at the coastal area of the Atacama Desert. Energies 13, 3819.
Olivares, D., Ferrada, P., de Matos, C., Marzo, A., Cabrera, E., Portillo, C., Llanos, J., 2017. Characterization of soiling on PV modules in the Atacama Desert. Energy Procedia 124, 547–553.
Osinergmin. (2024, April). *Organismo Supervisor de la Inversión en Energía y Minería*. Retrieved from ⟨https://www.osinergmin.gob.pe/seccion/centro_documental/electricidad/Documentos/Publicaciones/Compendio-Proyectos-CGENC-EPO-aprobados-COES.pdf⟩.
Piliougine, M., Guejia-Burbano, R.A., Petrone, G., Sánchez-Pacheco, F.J., Mora-López, L., Sidrach-de-Cardona, M., 2021. Parameters extraction of single diode model for degraded photovoltaic modules. Renew. Energy 164, 674–686.
Proietti, A., Panella, M., Leccese, F., Svezia, E., 2015. Dust detection and analysis in museum environment based on pattern recognition. Measurement 66, 62–72.
Rahman, M.M., Selvaraj, J., Rahim, N.A., Hasanuzzaman, M., 2018. Global modern monitoring systems for PV based power generation: A review. Renew. Sustain. Energy Rev. 82, 4142–4158.
Rezvanyvardom, M., Mirzaei, A., 2020. High gain configuration of modified ZVT SEPIC-Boost DC-DC converter with coupled inductors for photovoltaic applications. Sol. Energy 208, 357–367.
Salas, V., Olias, E., Barrado, A., Lazaro, A., 2006. Review of the maximum power point tracking algorithms for stand-alone photovoltaic systems. Sol. Energy Mater. Sol. Cells 90, 1555–1578.
Senniappan, G., Umapathy, P., 2021. A novel hybrid human psychology optimization-perturb and observe MPPT algorithm in a dsPIC microcontroller for grid connected PV power system. J. Intell. Fuzzy Syst. 41, 3011–3030.
Senthilkumar, S., Mohan, V., Deepa, R., Nuthal Srinivasan, M., Kumar, T.S., Thanikanti, S.B., Prathap, N., 2023. A Review on MPPT Algorithms for Solar PV Systems. Int. J. Res. -GRANTHAALAYAH 11, 25–64.
Sevillano-Bendezú, M.A., Pleshcheva, V., Calsi, B., Conde, L.A., Montes-Romero, J., Aguilera, J., de la Casa, J., Töfflinger, J.A., 2024. Assessing the accuracy of analytical methods for extracting parameters of different PV module technologies under clear and cloudy sky conditions. Energy Reports 12, 4279–4293.
Shang, L., Guo, H., Zhu, W., 2020. An improved MPPT control strategy based on incremental conductance algorithm. Prot. Control Mod. Power Syst. 5, 1–8.
Sivamani, S., Mohan, V., 2022. A Three-Phase Reduced Switch Count Multilevel Inverter Topology. Int. Trans. Electr. Energy Syst. 2022.
Smestad, G.P., Germer, T.A., Alrashidi, H., Fernández, E.F., Dey, S., Brahma, H., et al., 2020. Modelling photovoltaic soiling losses through optical characterization. Sci. Rep. 10, 58.
Spanoche, S.A., Stewart, J.D., Hawley, S.L., & Opris, I.E. (2012). Model-based method for partially shaded PV modules hot spot suppression. *2012 IEEE 38th photovoltaic specialists conference (PVSC) PART 2*, (pp. 1–7).
Sze, V., Chen, Y.-H., Yang, T.-J., Emer, J.S., 2020. Efficient processing of deep neural networks. Springer.
Thakurta, S.G. (2020). A modified MPPT algorithm for single phase grid connected PV system. *2020 National Conference on Emerging Trends on Sustainable Technology and Engineering Applications (NCETSTEA)*, (pp. 1–6).
Tieleman, T., Hinton, G., et al., 2012. Lecture 6.5-rmsprop: Divide the gradient by a running average of its recent magnitude. COURSERA: Neural Netw. Mach. Learn. 4, 26–31.
Vásquez, P., Palma-Behnke, R., & Devoto, I. (2019). Analysis of failure and degradation modes of small-scale photovoltaic power plants in rural communities of the atacama desert. *Proc. ISES Solar World Congr, 2019*, 2514–2525.
Walker, G., 2001. Evaluating MPPT converter topologies using a MATLAB PV model. J. Electr. Electron. Eng., Aust. 21, 49–55.
Zaihidee, F.M., Mekhilef, S., Seyedmahmoudian, M., Horan, B., 2016. Dust as an unalterable deteriorative factor affecting PV panel's efficiency: Why and how. Renew. Sustain. Energy Rev. 65, 1267–1278.
Zhang, L., Li, Y., Zhang, H., Xu, X., Yang, Z., Xu, W., 2021. A review of the potential of district heating system in Northern China. Appl. Therm. Eng. 188, 116605.
Zhang, C., Shen, C., Yang, Q., Wei, S., Lv, G., Sun, C., 2020. An investigation on the attenuation effect of air pollution on regional solar radiation. Renew. Energy 161, 570–578.
Zhao, Y., An, A., Xu, Y., Wang, Q., Wang, M., 2021. Model predictive control of grid-connected PV power generation system considering optimal MPPT control of PV modules. Prot. Control Mod. Power Syst. 6, 1–12.